Equatorially forced intraseasonal propagations along the Peru-Chile coast and their relation with the nearshore eddy activity in 1992–2000: A modeling study

Ali Belmadani,[1,2,3] Vincent Echevin,[1] Boris Dewitte,[2,4] and François Colas[1]

Received 20 December 2011; revised 25 February 2012; accepted 29 February 2012; published 14 April 2012.

[1] A regional eddy-resolving oceanic model spanning the 1992–2000 period is used to study the influence of 50 to 80 day intraseasonal equatorial Kelvin waves (IEKW) on mesoscale eddy activity off the west coast of Peru and northern and central Chile. The model is shown to realistically simulate nearshore intraseasonal sea level variability, poleward propagation of equatorially forced coastal trapped waves along the coastal waveguide, and offshore variability related to mesoscale eddies and Rossby waves (RW). In agreement with linear theory, RW are confined equatorward of ∼12°S in the 50–80 days period range. South of that critical latitude, westward propagation is dominated by energetic mesoscale signals resulting mainly from coastal flow instability. Sensitivity experiments to the open boundary conditions are then used to estimate to what extent eddy activity is impacted by the remote equatorial forcing. A coastal increase in eddy kinetic energy related to the energetic 60 day IEKW activity present in the open boundary forcing is evidenced and is largest off northern Peru, whereas no major changes are observed offshore. Additional regional simulations with different open boundary conditions corroborate our findings and suggest that this limited effect of IEKW on the offshore eddy kinetic energy may be a robust feature.

Citation: Belmadani, A., V. Echevin, B. Dewitte, and F. Colas (2012), Equatorially forced intraseasonal propagations along the Peru-Chile coast and their relation with the nearshore eddy activity in 1992–2000: A modeling study, *J. Geophys. Res.*, *117*, C04025, doi:10.1029/2011JC007848.

1. Introduction

[2] The Humboldt Current System (HCS), also known as the Peru-Chile coastal upwelling system, is the Eastern Boundary Upwelling System (EBUS) of the South Pacific Ocean. Persistent alongshore trade winds blowing off the west coast of South America drive strong coastal upwelling of cold, nutrient-rich waters [*Strub et al.*, 1998] that sustain high biological productivity [*Chavez*, 1995] together with the most productive marine ecosystem in the world ocean [*Chavez et al.*, 2008; *Food and Agriculture Organization*, 2009].

[3] A singularity of the HCS compared to other EBUSs is its proximity to the equator. In particular, the coastline and continental slope morphology make the HCS very sensitive to equatorial variability, at time scales ranging from intraseasonal [*Brink*, 1982; *Enfield*, 1987; *Spillane et al.*, 1987; *Shaffer et al.*, 1997; *Clarke and Ahmed*, 1999; *Hormazabal et al.*, 2002; *Camayo and Campos*, 2006; *Dewitte et al.*, 2011] and seasonal [*Pizarro et al.*, 2002; *Ramos et al.*, 2006; *Dewitte et al.*, 2008a] to interannual [*Pizarro et al.*, 2001, 2002; *Vega et al.*, 2003; *Ramos et al.*, 2008] and decadal [*Montecinos et al.*, 2007]. Of particular interest are the intraseasonal equatorial Kelvin waves (IEKW) in the $(50–80\ \text{days})^{-1}$ frequency range. Such waves are very energetic along the equator [*Kessler et al.*, 1995; *Cravatte et al.*, 2003; *Dewitte et al.*, 2008b] because of the characteristics of the high-frequency tropical Pacific atmospheric forcing, which is dominated by the Madden and Julian Oscillation (MJO) [*Madden and Julian*, 1971, 1972]. According to linear theory [*Clarke and Shi*, 1991] (hereafter CS91), IEKW are easily trapped along the coast where they propagate as free coastal trapped waves (CTW). Indeed, such theory predicts that part of the wave energy transmitted along the equator by equatorial Kelvin waves (EKW) is reflected at the eastern boundary of the basin as Rossby waves (RW), whereas the rest is trapped at the coast in the form of CTW. In addition, for a Kelvin wave oscillating at a given frequency, there exists a critical latitude for each baroclinic mode that determines whether free wave motion is trapped or reflected: reflection occurs equatorward of that latitude, whereas unforced motion is trapped poleward of it [*Clarke*, 1983; *Grimshaw and Allen*, 1988; CS91]. The higher the frequency and/or the higher the vertical mode, the lower the critical latitude. According to CS91, for 50 to 80 day IEKW, the critical latitude ranges from 7°S to 10°S

[1]LOCEAN/IRD/IPSL/UPMC, Paris, France.
[2]LEGOS/IRD/OMP/UPS, Toulouse, France.
[3]Now at International Pacific Research Center, School of Ocean and Earth Science and Technology, University of Hawai'i at Mānoa, Honolulu, Hawaii, USA.
[4]IMARPE, Callao, Peru.

0148-0227/12/2011JC007848

Table 1. The ROMS Simulations Considered in This Study[a]

ROMS Simulation	OBC Model Name	OBC Time Averaging	Ensemble Members
R5d	ORCA	5 days	10
R1m	ORCA	1 month	10
R5d-SODA	SODA	5 days	10
R1m-SODA	SODA	1 month	10

[a]ROMS, Regional Ocean Modeling System; OBC, open boundary conditions; SODA, Simple Ocean Data Assimilation.

for the first baroclinic mode and is lower than 6°S for higher-order modes.

[4] CTW have a noticeable impact on coastal hydrography and currents [*Shaffer et al.*, 1997; *Clarke and Ahmed*, 1999; *Hormazabal et al.*, 2002, 2006], particularly the poleward Peru-Chile undercurrent (PCUC), which constitutes a main source for waters upwelled near the coast [*Strub et al.*, 1998; *Montes et al.*, 2010]. Seasonal CTW modify vertical shears between the PCUC and the equatorward surface jet, the Chile-Peru coastal current (CPCC), thus modulating baroclinic instabilities [*Echevin et al.*, 2011] and thereby the nearshore generation of westward propagating mesoscale eddies. Furthermore, intraseasonal CTW can modulate nutrient uptake at the surface and thereby have a strong influence on marine primary production (V. Echevin et al., Remotely forced intraseasonal variability of the Northern Humboldt Current System surface chlorophyll using a coupled physical-ecosystem model, unpublished manuscript, 2012) and supposedly the pelagic ecosystem [*Bertrand et al.*, 2008]. However, the detailed mechanisms of intraseasonal CTW impact on eddy activity have not been documented yet for the Peru-Chile coast.

[5] The present study aims at characterizing the intraseasonal CTW propagating along the coast of Peru (4°S–18°S) and Chile (18°S–35°S) and assessing their influence on mesoscale eddy activity in the nearshore and offshore HCS region using a nonlinear regional ocean circulation model. It focuses on a time period that experienced a strong IEKW activity, namely 1992–2000, particularly in the form of downwelling IEKW associated with westerly wind bursts (WWB) blowing over the western Pacific warm pool [*McPhaden*, 1993; *Kessler and McPhaden*, 1995; *Kessler et al.*, 1995]. The approach is based on experiments that measure sensitivity to the open boundary conditions (OBC) of the regional model. It takes advantage of a vertical mode decomposition of the model variability to interpret the results in the light of the linear formalism, similarly to *Dewitte et al.* [2008a]. An eddy kinetic energy (EKE) budget is estimated following *Marchesiello et al.* [2003] in order to detail the mechanism of EKE change due to IEKW forcing.

[6] The paper is organized as follows: in section 2, the regional model and the open boundary forcings are presented, together with the observed data used for model validation. The methods used in the paper are also described in this section. The regional model mean state and variability are validated against observations and the existing literature in section 3. Section 4 describes the propagation characteristics of IEKW, RW and CTW in the model. In section 5, the sensitivity experiments to the remote intraseasonal forcing are analyzed in the light of the estimation of baroclinic and barotropic instabilities as well as wind work. The robustness of the results is shown in section 6, by repeating some of the analyses with a different open boundary forcing. Section 7 summarizes the results before concluding.

2. Models, Observations, and Methods

2.1. Numerical Models

2.1.1. Regional Ocean Modeling System

[7] The Regional Ocean Modeling System (ROMS) regional ocean circulation model [*Shchepetkin and McWilliams*, 2005] is used at an eddy-resolving resolution (1/6° at the equator) in a study region extending from 15°N to 40°S, and from the coast to 100°W, with lateral open boundaries on its northern, western and southern sides. ROMS solves the hydrostatic primitive equations with a free-surface explicit scheme, and stretched, terrain-following sigma coordinates on 32 vertical levels. Subgrid-scale vertical mixing is parameterized using the KPP boundary layer scheme [*Large et al.*, 1994]. Bottom topography from ETOPO2 [*Smith and Sandwell*, 1997] has been interpolated onto the model grid and smoothed following *Penven et al.* [2005] in order to reduce pressure gradient errors. 5-daily oceanic outputs from the ORCA05 model (1/2° resolution) [*Madec et al.*, 1998] or from the Simple Ocean Data Assimilation (SODA) 2.3.0 reanalysis (1/2° resolution) [*Carton and Giese*, 2008] provide the OBC for temperature, salinity, horizontal velocity, and sea level over the period 1992–2000. They were treated using a combination of an Orlanski scheme for the tracers and for baroclinic velocities, and a Flather scheme for the barotropic mode [*Marchesiello et al.*, 2001]. Initial conditions are from climatological values derived from a 1992–2000 simulation performed with the ORCA (C. Ethée, unpublished data, 2003) and the SODA model. To force the regional model at the air/sea interface, wind stress from the ERS1–2 satellite scatterometer measurements (50 km resolution) [*Bentamy et al.*, 1996] and fluxes (heat, freshwater, solar shortwave radiation) from the European Center for Medium-Range Weather Forecasts (ECMWF) ERA-40 global atmospheric reanalysis (1.25° resolution) [*Uppala et al.*, 2005] were used. Monthly means were chosen for the surface forcing in order to damp atmospheric intraseasonal variability and thereby focus on the effect of intraseasonal variability originating from the lateral open boundary forcing on the model solution. Heat fluxes include a Newtonian restoring term to Reynolds 1° weekly interannual sea surface temperature (SST) [*Reynolds and Smith*, 1994] and to COADS 1° monthly climatological sea surface salinity fields [*Da Silva et al.*, 1994].

[8] The atmospheric forcing, initial and boundary conditions were linearly interpolated onto the ROMS grid using the ROMSTOOLS software [*Penven et al.*, 2008]. A 2 year spin-up was performed with climatological values derived from the forcing and the boundary conditions, after which model outputs were saved every 5 days from 1st January 1992 onward. The simulation with ORCA (SODA) boundary forcing is hereafter referred to as R5d (R5d-SODA) (Table 1).

[9] To assess the sensitivity of the model solution to the intraseasonal open boundary forcing, similar ROMS simulations were performed, except that monthly means derived from the ORCA/SODA simulations were used at the open boundaries of the regional domain in order to damp the IEKW variability. Unless otherwise stated, the IEKW is

Table 2. Modeled and Observed Intraseasonal Sea Level Variability at the Equator and Near the Peru Coast[a]

	Intraseasonal SLA Standard Deviation (cm)		
	0°N, 100°W (IEKW)	0°N, 95°W	10°S, 78.3°W
R5d	1.23	1.47	1.72
R1m	0.64	0.98	0.96
ORCA (5-daily)	1.23	1.61	1.86
ORCA (monthly)	0.64	0.92	0.82
SODA (5-daily)	1.15	1.89	1.87
SODA (monthly)	0.60	1.43	1.17
AVISO	–	2.57	2.56

[a]Note that since the intraseasonal equatorial Kelvin waves (IEKW) computation relies on the availability of the mean stratification profile, it could not be assessed from the altimetric data. SLA, sea level anomalies; AVISO, Archiving, Validation, and Interpretation of Satellite Oceanographic data.

diagnosed here as the summed contributions of the first three baroclinic modes to equatorial sea level (see 2.3 for a description of the method used to derive IEKW), high-pass-filtered with a 90 day cutoff period. The IEKW standard deviation at 100°W in the ORCA/SODA monthly means (0.64/0.60 cm) is indeed half of that in the ORCA/SODA 5-daily outputs (1.23/1.15 cm) (Table 2). The atmospheric forcing is the same as in R5d or R5d-SODA. These ROMS simulations are hereafter referred to as R1m and R1m-SODA (Table 1).

2.1.2. ORCA

[10] The primitive equation ORCA05 model [*Madec et al.*, 1998] is used to provide OBC for ROMS. ORCA05 is an ocean general circulation model (OGCM) with 1/2° resolution and 31 z levels in the vertical, with 10 m intervals between 0 and 100 m, and 500 m at 4750 m depth. The OGCM is forced by ERS1–2 winds, NCEP heat fluxes [*Kalnay et al.*, 1996] and CMAP freshwater fluxes [*Xie and Arkin*, 1996] following *Lengaigne et al.* [2002].

2.1.3. SODA

[11] The SODA ocean reanalysis [*Carton and Giese*, 2008] is also used as OBC for ROMS, with the purpose of assessing the robustness of the results obtained with ORCA as OBC (see section 6). SODA uses an OGCM based on the Parallel Ocean Program (POP) [*Smith et al.*, 1992] with 1/2° resolution and 40 vertical z levels with 10 m spacing near the surface, and 250 m at 5374 m depth. Assimilated data include temperature and salinity profiles from the World Ocean Database 2001 [*Boyer et al.*, 2002; *Stephens et al.*, 2002; *Locarnini et al.*, 2002], as well as additional hydrography, SST, and altimeter sea level. The model was forced by ERA-40 winds and heat fluxes, and Global Precipitation Climatology Project freshwater fluxes (GPCP) [*Adler et al.*, 2003].

2.2. Observed Data

2.2.1. CSIRO Atlas of Regional Seas

[12] Climatological data from the CSIRO Atlas of Regional Seas (CARS) 2009 [*Ridgway et al.*, 2002; *Dunn and Ridgway*, 2002] were used to validate the model temperature and salinity near the coast. Unlike other climatologies, CARS uses an adaptive length scale mapper that takes topographic barriers into account. For every mapped point, a 3D ellipse is computed that provides 400 data points at that depth. As a result, length scales are automatically adapted to the density of in situ data, with maximum resolution in data-rich areas. The higher resolution of the gridded CARS climatology (1/2°) and a specific treatment taking steep bathymetry into account make it more appropriate for our study region compared to other products.

2.2.2. Archiving, Validation, and Interpretation of Satellite Oceanographic Data

[13] The sea levels simulated by ROMS are compared to Archiving, Validation, and Interpretation of Satellite Oceanographic data (AVISO) satellite altimetric data (http://www.aviso.oceanobs.com/) available from October 1992 to December 2000. Weekly data available on a 1/3° gridded field result from optimal interpolation of combined altimetric data from Topex/Poseidon and ERS1–2 satellites [*Le Traon et al.*, 1998].

2.3. Methodology

2.3.1. Space-Time Analysis

[14] The propagating nature and spatiotemporal characteristics of IEKW and RW are diagnosed using a wavelength-frequency decomposition [*Hayashi*, 1979, 1982]. This bivariate space-time analysis consists in the projection of a unidimensional data set varying over time onto a selected number of wavelengths (four traveling wave numbers and stationary waves in this case) for both possible directions of propagation (east/west for IEKW and RW), followed by a discrete Fourier transform of the resulting time series associated with each wavelength. Applied to high-pass-filtered sea level anomalies (SLA), it allows separating standing and propagating oscillations and identifying their direction of propagation (if any), dominant frequencies and associated wavelengths. Note that here SLA refers to the sea level signal from which time-mean average was removed. RW propagation was diagnosed along zonal sections separated by 1° intervals from the equator to 35°S. The sections have a fixed length and are limited to the east by the coastline. The length was chosen to be equal to that of the section between the western boundary and the westernmost grid point on land south of the equator (located around 81.5°W, 5°S). The southern boundary (40°S) was excluded from the analysis because of the side effects associated with the sponge layer used at the open boundaries.

[15] Unless specified, the term "anomalies" refers here to the total 5-daily signal from which a monthly climatology interpolated (using a spline function) onto a 5-daily temporal grid was removed. Anomalies are thus considered as departures from climatological values that only contain low-frequency components of the signal such as the annual and semiannual harmonics. In the following, intraseasonal anomalies refer to the high-pass-filtered anomalies with a 150 day cutoff frequency, since we focus on time scales of periodicity lower than 120 days: indeed, the preferential intraseasonal frequency band along the equator features long-wavelength Kelvin waves at ~50, 70, and 100 days [*Dewitte et al.*, 2008b].

2.3.2. Estimation of the CTW Spatial Structure

[16] To characterize the alongshore, cross-shore and vertical structures of CTW, empirical orthogonal functions (EOFs) are computed over cross-shore vertical sections of the alongshore current anomalies every 5° of latitude from 5°S to 35°S. A band-pass filter was previously applied to the anomalies in order to extract different frequencies of interest

within the (50–120 days)$^{-1}$ intraseasonal frequency band, which were identified from space-time analysis. Note that cutoff frequencies used for band-pass filtering throughout the paper are equal to the frequency of interest ± 10 days. Cross-shore direction was determined at each latitude from the coastline angle θ. The latter was estimated at each latitude from the position of the coastline defined by the land-sea mask: the resulting angle was smoothed in order to reduce noise originating from model resolution and from the contour of the land-sea mask.

[17] The EOF calculation is performed over the grid points located inside the first baroclinic mode Rossby radius of deformation (typically 3–4 grid points). The objective is to capture the vertical structure variability of CTW only and avoid contamination associated with RW variability that radiates offshore. Once the EOFs are performed, spatial patterns and frequency spectra of the time series associated with the principal components (PCs) are analyzed in order to identify coastally trapped structures oscillating at the frequency of interest. Time series of such structures are then lag correlated in order to track coherent poleward propagation along the coast.

2.3.3. Vertical Mode Decomposition

[18] A vertical mode decomposition of the model mean stratification is performed in order to derive baroclinic mode contributions to sea level and current anomalies. To derive the IEKW, the ORCA/SODA mean stratification along the equator is used to derive the vertical modes at each longitude. The corresponding meridional modes are used to derive the amplitude of the Kelvin wave of a particular baroclinic mode by projecting both current and SLA contributions to this mode. The method is similar to the one of *Dewitte et al.* [2003]. For the eastern South Pacific domain, the baroclinic modes are derived at each grid point from the mean stratification as simulated by ROMS. The method is detailed by *Dewitte et al.* [2008a]. The baroclinic modes can be used to interpret the simulated variability within the linear formalism and compare our results with those predicted from CS91's theory. The decomposition was applied to the entire regional domain so as to describe the vertical structure of the anomalies related to IEKW and RW in the regional model solution. In addition, a 2° coastal band extending from the latitude of the Galapagos islands (1.4°S) to the southern boundary was used to assess some characteristics of CTW activity.

[19] The limitations of the method were discussed by *Dewitte et al.* [2008a] and *Ramos et al.* [2008]. Briefly, we assumed that linearization and that the Wentzel-Kramers-Brillouin (WKB) approximation were appropriate. The former requires small interface deviations compared to mean layer thickness, which should be true on intraseasonal time scales: the amplitude of IEKW-induced thermocline depth variations derived from TAO measurements at 95°W [*McPhaden et al.*, 1998] is about 10% of the mean value [*Cravatte et al.*, 2003; *Jiang et al.*, 2009]. At higher latitudes, the thermocline is shallower, but equatorially forced intraseasonal variability is also expected to be weaker because of dissipation and RW radiation at lower latitudes. The WKB approximation requires that the length scale of background state changes is large compared to that of the perturbations: in fact, the joint influence of bottom topography and varying stratification on baroclinic modes and their phase speeds is significant near the coast but weak in the inner basin [*Killworth and Blundell*, 1999]. Caution is therefore required for the interpretation of the results obtained from the coastal area.

2.3.4. Eddy Kinetic Energy Budget

[20] A simplified EKE budget is calculated to diagnose the source terms for eddy activity in the model. Here we use surface EKE computed from geostrophic velocity anomalies derived from sea level variations as a measure of eddy activity, which is commonly used for this purpose [e.g., *Marchesiello et al.*, 2003; *Capet et al.*, 2008]. Following *Marchesiello et al.* [2003] who performed such budget in a ROMS configuration of the California Current System, we focus on energy conversion terms relevant to nearshore EKE generation in the model, which are

Wind work

$$F_e K_e = \frac{\overline{u'\tau_x'} + \overline{v'\tau_y'}}{\rho_0} \tag{1}$$

where u and v are the zonal and meridional surface currents, respectively, $\boldsymbol{\tau}_x$ and $\boldsymbol{\tau}_y$ are the zonal and meridional surface wind stresses, respectively, ρ_0 is mean seawater density, prime marks denote anomalies, and overbars denote time-mean averages;

Barotropic instability

$$K_m K_e = -\left(\overline{u'u'}\frac{\partial \overline{u}}{\partial x} + \overline{u'v'}\frac{\partial \overline{u}}{\partial y} + \overline{u'w'}\frac{\partial \overline{u}}{\partial z} + \overline{v'u'}\frac{\partial \overline{v}}{\partial x} + \overline{v'v'}\frac{\partial \overline{v}}{\partial y} + \overline{v'w'}\frac{\partial \overline{v}}{\partial z}\right) \tag{2}$$

where u, v, and w are the zonal, meridional, and vertical currents, respectively, and x, y, and z are the zonal, meridional, and vertical directions, respectively; and

Baroclinic instability

$$P_e K_e = \frac{-g}{\rho_0}\overline{\rho' w'} \tag{3}$$

where ρ is density and g is the acceleration due to gravity.

[21] $F_e K_e$ represents the transfer of energy from surface wind-forcing anomalies to EKE, $K_m K_e$ represents the barotropic conversion from mean kinetic energy to EKE, and $P_e K_e$ represents the baroclinic conversion from eddy available potential energy to EKE.

[22] Each of the three conversion terms was computed at each model grid point (at the free surface for wind work). Barotropic and baroclinic instability terms were then integrated over the first 100 m depth, where most simulated nearshore instabilities along the coast of Peru and Chile are confined [see *Colas et al.*, 2012, Figure 9], in order to be directly comparable to wind work. Finally, each conversion term was alongshore-averaged in the latitude ranges where EKE changes were observed. The reader is invited to refer to *Marchesiello et al.* [2003] for more details about the method, which offers an effective and synthetic way to diagnose the source and transfers of EKE in upwelling systems.

2.3.5. Statistical Significance

[23] To provide statistically significant results in terms of the differences in EKE between the two simulations,

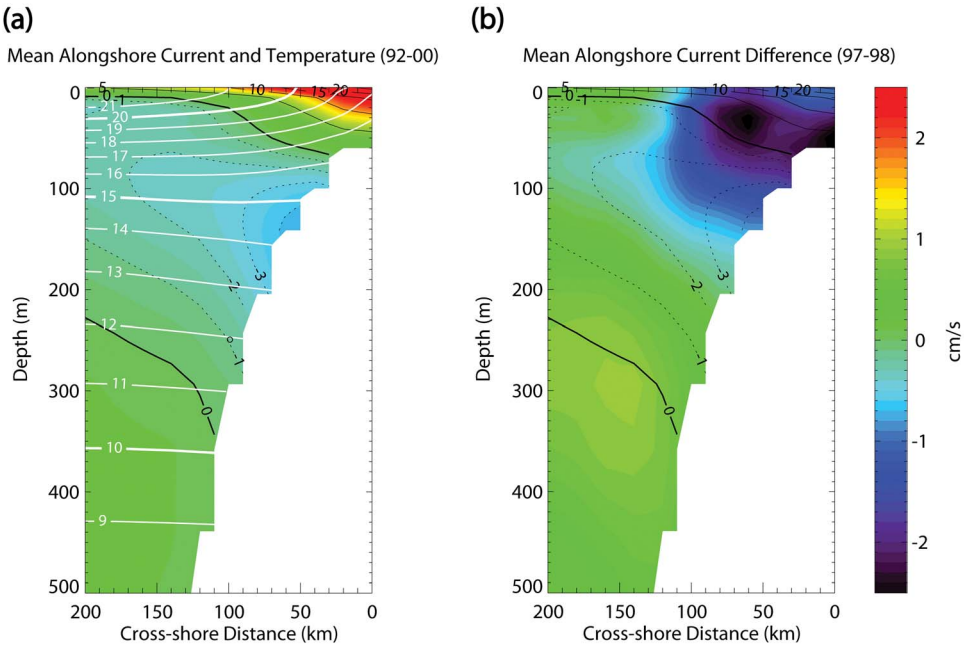

Figure 1. (a) Mean alongshore current and temperature from R5d over 1992–2000, alongshore-averaged between 7°S and 13°S, as a function of seaward cross-shore distance (km) and depth (m). Units are cm/s (°C) for the alongshore current (temperature). Shading and black lines are for the alongshore current (dashed lines are for negative values, i.e., for poleward flow), and white lines are for temperature. (b) Difference between the mean alongshore current from R5d over January 1997 to June 1998 and that over 1992–2000 (shading) and mean alongshore current over 1992–2000 (contours). Positive (negative) values are for equatorward (poleward) current or current difference.

ensemble experiments with perturbed initial conditions were performed for each model configuration (R5d/R5d-SODA and R1m/R1m-SODA). That is, for both R5d and R1m (R5d-SODA and R1m-SODA), ten simulations were run with different initial conditions. These were provided by the January 1st outputs from a 15 year simulation with climatological forcing following *Penven et al.* [2005] and *Echevin et al.* [2011]. The mean EKE difference was then defined as the difference between the ensemble mean from R5d/R5d-SODA and the ensemble mean from R1m/R1m-SODA (10 members for each configuration).

[24] To assess the statistical significance of such ensemble mean difference, a bootstrap method [*Efron and Tibshirani*, 1994] was applied. First, model output differences from the ensemble members (i.e., R5d-R1m for each member) were subsampled in the time domain with the purpose of deriving independent and identically distributed (hereafter iid) realizations of EKE difference. The subsampling was obtained by using a typical decorrelation time, estimated from the lag at zero crossing of the autocorrelation function of the considered variable. To reduce the noise related to the spatial variations of the decorrelation time over the study region, the estimated values for the decorrelation time were area-averaged over an open ocean subdomain (100°W–74°W, 40°S–18°S) and a coastal/tropical subdomain (the rest of the domain): indeed, the decorrelation time for EKE difference was found to be ~95 days (~55 days) on average over the former (latter) region (see Figure 10b). This is consistent with the dominance of relatively fast baroclinic wave response along the equatorial and coastal waveguides, and slower RW/mesoscale eddy activity in the subtropics. Hence, subsampling the ten ensemble members for each configuration (10 × 9 years with 5-daily time step) allowed considering 597 iid realizations for the coastal/tropical subdomain and 345 iid realizations for the open ocean subdomain.

[25] Then, the iid realizations were randomly resampled with replacement using a Monte Carlo technique. The operation was repeated 1000 times in order to derive a bootstrap distribution of the ensemble mean EKE difference. The 2.5th and 97.5th percentiles were then used to infer 95% confidence intervals at each grid point. The ensemble mean difference was considered significant at the 95% level if it was within the 95% confidence interval.

3. Model Validation

[26] In this section, some characteristics of the modeled mean state and variability are compared to the available observations and to the existing literature in order to validate the use of ROMS for the study of the influence of IEKW on mesoscale activity in the region.

3.1. Mean State

[27] In terms of mean state, the focus is on the vertical structure of temperature, salinity and alongshore currents near the coast, and on mesoscale eddy activity. The mean stratification influences CTW propagation, whereas alongshore current shear controls to some extent baroclinic instabilities (and the associated eddy activity), so that these features need to be simulated realistically by the model.

[28] Figure 1a presents the simulated mean cross-shore vertical structure of temperature and alongshore currents,

alongshore-averaged over the relatively straight central Peru coast (7°S–13°S). As expected, isotherms are tilted upward in the first ∼100 km from the coast and within a ∼100 m thick surface layer. The cross-shore extent of the simulated coastal upwelling is of the order of the Rossby radius of deformation at this latitude range (∼100 km [*Chelton et al.*, 1998]). Since the latter determines the cross-shore scale of CTW, and since baroclinic mode phase speeds of CTW propagation directly depend on local stratification, a realistic representation of coastal upwelling appears essential for the simulation of CTW propagation. The rise of the isotherms creates a cross-shore density gradient driving a geostrophic equatorward CPCC, with velocities over 20 cm/s near the coast (Figure 1a). The poleward PCUC is found below the CPCC, with its core located over the continental shelf and slope at ∼150 m depth, making it a primary source for the upwelled waters. Velocities in the core of the PCUC reach ∼4–5 cm/s.

[29] These velocity patterns may be compared to those observed at 10°S by *Huyer et al.* [1991, Figure 11; see also *Strub et al.*, 1998, Figure 10.3] from four surveys in the period 1982–1983, which are among the scarce observations available in this region. The modeled velocities are qualitatively consistent with those observed by *Huyer et al.* [1991]: the latter feature a thin surface equatorward flow extending ∼150–200 km offshore and strongest near the coast, together with a subsurface poleward flow located directly underneath the former and attached to the continental shelf break. However, the modeled CPCC is stronger (∼25 cm/s) than observed (∼14 cm/s), whereas the modeled PCUC is weaker (∼4.5 cm/s and 18 cm/s in ROMS and in the observations, respectively). This may be due to a bias in the ERS winds nearshore wind stress curl (see below). Nevertheless, the comparison is limited by the fact that the data used by *Huyer et al.* [1991] correspond to a peculiar period characterized by the strong 1982–1983 El Niño, so that such observations might not reflect the long-term mean structure of the coastal currents. Indeed, time-averaged simulated alongshore currents during the 1997–1998 El Niño, which was of comparable intensity to the 1982–1983 El Niño, display a weaker CPCC by ∼2–3 cm/s (∼10%–20%) and a more intense PCUC by ∼1–2 cm/s (∼20%–50%) compared to the 1992–2000 averages (Figure 1b). In addition, the velocities of the coastal currents vary strongly with latitude (not shown) because of alongshore changes in topography, coastline effects, and interaction with eddies at eddy generation locations, which further limits quantitative comparisons with the data of *Huyer et al.* [1991].

[30] We also compare our results to other studies of the HCS based on ROMS simulations at 1/6° [*Albert et al.*, 2010] and 1/9° [*Penven et al.*, 2005; *Montes et al.*, 2010; *Echevin et al.*, 2011]. Apart from model resolution, the main differences in model configuration are the horizontal extent of the domain (90°W–70°W, 20°S–3°N versus 100°W–70°W, 40°S–15°N here), the atmospheric forcing (climatological versus interannual here) and the ocean initial and boundary conditions provided by ORCA in our case. *Albert et al.* [2010] used both ERS and QuikSCAT winds to force their model and assessed the associated sensitivity of the coastal currents. The vertical thermal structure is close to *Penven et al.* [2005, Figure 6c]: from ∼9°C at 500 m depth to ∼21°C at sea surface. However, the vertical gradient shown by *Penven et al.* [2005] is weaker in the upper 100 m compared to this study. Noteworthy, thermal stratification is sensitive to the initial and open boundary conditions [*Montes et al.*, 2010; *Echevin et al.*, 2011]. With SODA boundary forcing, the authors find a similar structure to the one presented here, except slightly cooler at the surface (∼20°C) and warmer at 400 m depth (∼11°C). *Albert et al.* [2010] also obtained a similar structure with ERS wind forcing, which appeared only slightly modified (cooler) with the higher-resolution QuikSCAT forcing.

[31] The coastal currents simulated by *Penven et al.* [2005] are also very similar to those we described: a thin CPCC in the surface layer with maximum velocities ∼20 cm/s in the first ∼50 km from the coast, and a PCUC core located on the shelf break at ∼100–150 m depth with maximum velocities ∼4–5 cm/s. At 12°S, the results shown by *Montes et al.* [2010] are qualitatively consistent with ours, though with a weaker CPCC (∼10 cm/s) and a stronger PCUC (∼10 cm/s), i.e., closer to *Huyer et al.*'s [1991] observations. A possible explanation for the strong CPCC and weak PCUC presented here is the weak nearshore wind stress curl in ERS winds compared to QuikSCAT winds [*Croquette et al.*, 2007], which *Montes et al.* [2010] use to force ROMS. Indeed, it is known that cyclonic coastal wind curl along an eastern boundary drives a poleward barotropic flow through the Sverdrup relation, which imprints the subsurface baroclinic flow, particularly the poleward undercurrent [*Marchesiello et al.*, 2003]. *Albert et al.* [2010] further showed that only QuikSCAT forcing and the associated strong cyclonic curl were able to generate realistic PCUC and CPCC amplitudes, conversely to ERS forcing. However, it should be noted that other factors such as large-scale background oceanic mean state and OBC can also influence the magnitude of coastal currents [*Echevin et al.*, 2011]: for instance, *Penven et al.* [2005] and *Montes et al.* [2010] use the same QuikSCAT-derived climatological wind forcing, but differ in their OBC.

[32] To assess the ability of the model in reproducing the hydrographic conditions off northern Chile (∼18°S–25°S), mean subsurface temperature and salinity were compared to the CARS climatology (Figure 2). The model features both permanent upwelling and poleward PCUC flow, as seen from the isotherm and isohaline tilts in the upper 100 m near the coast and from the local subsurface salinity maximum along the shelf break in the 100–300 m depth range, respectively. Although ROMS tends to overestimate subsurface salinity by up to 0.1 PSU, all four water masses described by *Blanco et al.* [2001] are found in both the model solution and climatological data: highly salty (>34.8 PSU) subtropical water (STW) in the top 30–40 m, relatively salty (∼34.7–34.8 PSU) equatorial subsurface water (ESSW) carried by the PCUC, fresh (∼34.5–34.6 PSU) subantarctic water (SAW) located offshore just above the PCUC, and deep water influenced by Antarctic intermediate water (AIW).

[33] Figure 3 presents the mean EKE (see section 2.3) pattern for the reference simulation (R5d) and for AVISO data. Local maxima of model EKE are found near the equator, along the coast of Peru down to 18°S, and to a less extent along the coast of Chile down to about 35°S. Off central Chile (25–35°S), eddy activity extends to the offshore region until about 80°W, conversely to Peru where eddy activity is mostly confined within a 400 km

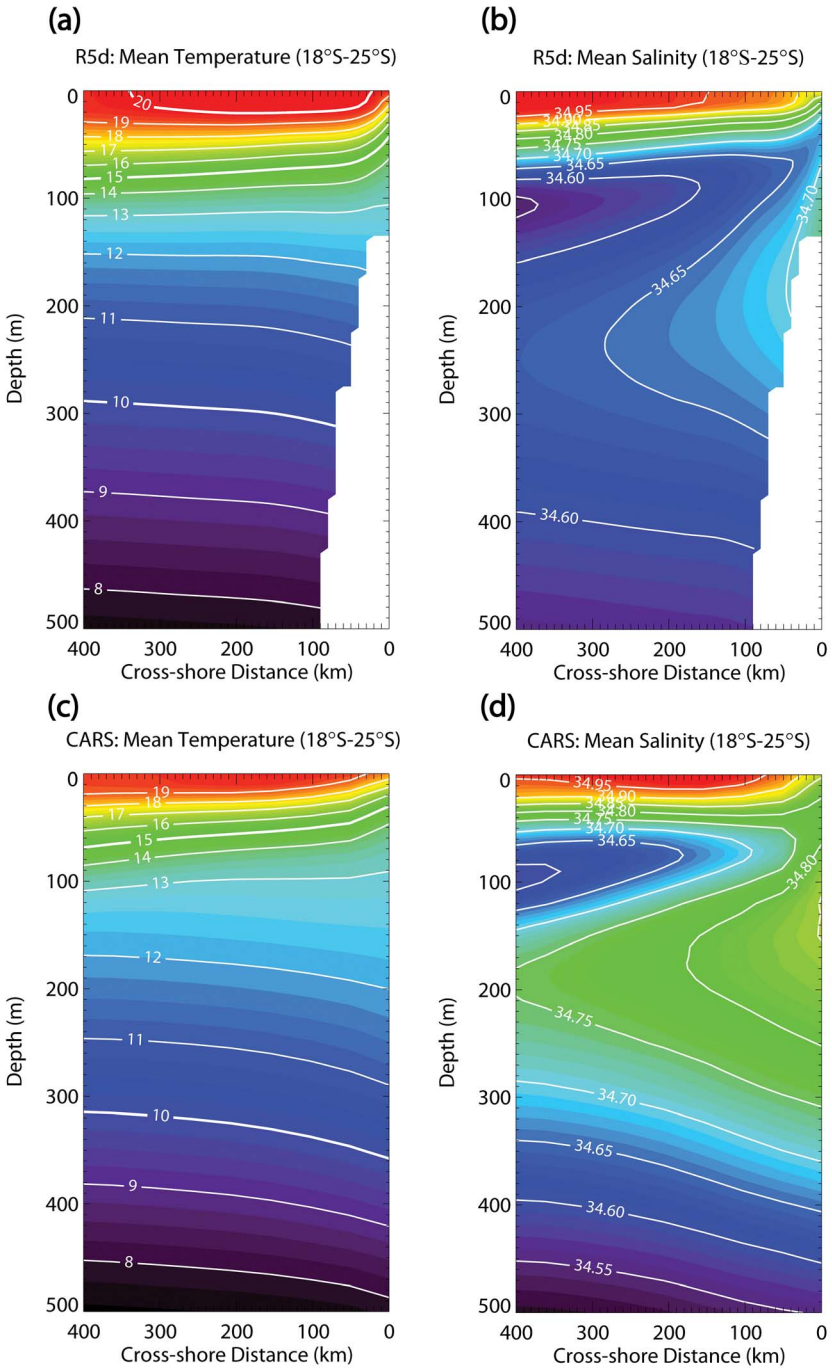

Figure 2. Annual mean (a) temperature and (b) salinity from R5d, alongshore-averaged between 18°S and 25°S, as a function of seaward cross-shore distance (km) and depth (m). (c and d) Same as Figures 2a and 2b, except for CSIRO Atlas of Regional Seas (CARS) climatological data. Units are °C and PSU for temperature and salinity, respectively.

wide coastal band. The simulated eddy activity agrees qualitatively with the observed: the latter also features local maxima off Chile, Peru, and in the equatorial band, together with similar energy levels over the region ($o(10)$ to $o(100)$ cm^2 s^{-2}). However, a notable discrepancy between the model solution and the observations is the underestimated EKE (~75–100 cm^2 s^{-2}) north of about 8°S compared to satellite data (~100–300 cm^2 s^{-2}). This may be due to the weaker than observed ORCA equatorial currents —for instance, *Belmadani* [2010] found mean velocities in the Equatorial Undercurrent (EUC) at 100°W of only ~0.4 m s^{-1}, about half the values found for SODA and for shipboard ADCP data—or variability (see section 3.2) or both. Another remarkable difference is the weak observed EKE in the first ~100 km from the coast outside the equatorial region (Figure 3c). This may be due to a limitation of

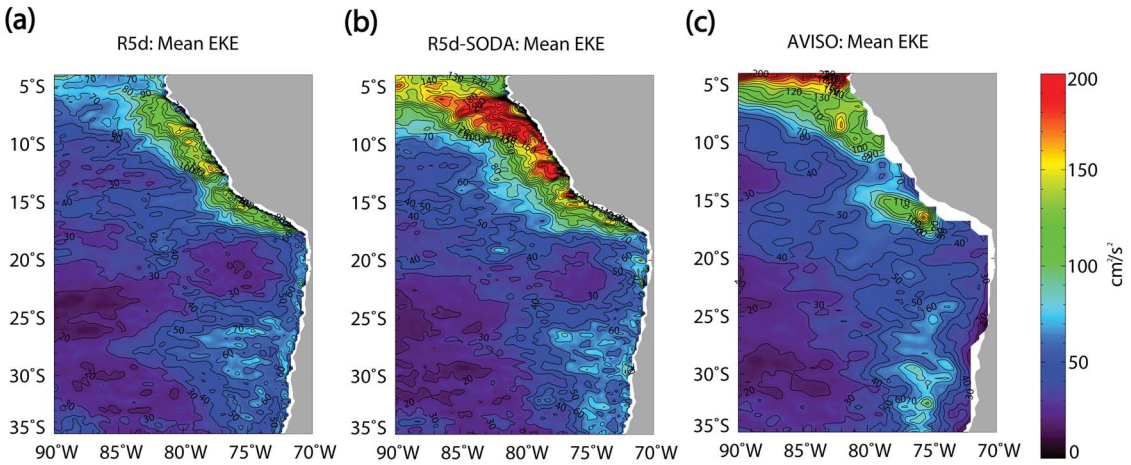

Figure 3. Annual mean eddy kinetic energy (EKE) computed from sea level anomalies (SLA) simulated in (a) R5d and (b) in R5d-SODA and (c) from Archiving, Validation, and Interpretation of Satellite Oceanographic data (AVISO) altimetric data. Units are cm^2/s^2. Contour interval (CI) is 10 cm^2/s^2.

satellite altimetry rather than to a model bias: as noted by *Capet et al.* [2008], nearshore mesoscale structures in EBUSs are generally too small to be detected (their typical radius is ∼20–50 km [see *Penven et al.*, 2005; *Chaigneau and Pizarro*, 2005; *Chaigneau et al.*, 2008]), whereas they grow in size while moving westward until they are detected and produce an offshore observed maximum. Furthermore, altimetric measurements are less accurate in the first ∼50 km from the coast because of various issues such as errors in the atmospheric and tidal corrections or land contamination in altimetric signals [e.g., *Volkov et al.*, 2007; *Bouffard et al.*, 2011].

3.2. Variability

[34] In order to assess the regional model remotely forced variability, equatorial SLA simulated by ROMS near the western boundary are compared to satellite altimetry (Figure 4a). The model simulation agrees well with the observed data (the correlation value between the two time series is 0.93). The signature of the 1997–98 El Niño event is clear in both the model and the observations and is associated with two positive peaks of SLA, previously described by several authors [*Blanco et al.*, 2002; *Strub and James*, 2002; *Colas et al.*, 2008], of successively ∼20 cm and ∼30 cm corresponding to intense EKW, values which are however ∼30% weaker than observed. The nonnegligible RMS misfit value (4.1 cm) is attributable to a large extent to these differences in the amplitudes of the El Niño peaks.

[35] In addition to the two El Niño peaks, the seasonal cycle is clearly distinguishable with an amplitude of ∼5–10 cm for both ROMS and AVISO data, and so is intraseasonal variability, with an amplitude of the order of a few centimeters. The latter is ∼40% weaker in ROMS (Table 2), which is mainly due to the ∼35% weaker than observed variability in the ORCA model (Table 2). Such underestimation is partly related to the 1997–98 El Niño (Figure 4a). A relatively good agreement between modeled and observed SLA was also found at 10°S near the coast of central Peru, which confirms the skill of the model in representing the observed remotely forced variability propagating poleward along the coastal waveguide (Figure 4b). Again, intraseasonal variability is underestimated by the ROMS model, although somewhat less (∼30%) than at the equator (Table 2).

4. The Propagation, Coastal Trapping, and Reflection of IEKW

[36] In the following, results from the regional model are used to describe the connection between IEKW, CTW and RW.

4.1. IEKW

[37] The propagation characteristics of the long IEKW present in the boundary forcing are assessed by applying space-time analysis to intraseasonal SLA from ORCA over the entire equatorial Pacific (Figure 5, thick solid line). The analysis clearly indicates the signature of the IEKW, with an eastward sea level propagation of basin-scale wavelength (∼16500 km), and typical frequencies around ω = (50–60 days)$^{-1}$, (70–80 days)$^{-1}$ and (120 days)$^{-1}$, consistently with AVISO data (Figure 5, thin dotted line) and earlier works [*McPhaden and Taft*, 1988; *Cravatte et al.*, 2003; *Dewitte et al.*, 2008b]. Note however that compared to altimetric data, the simulated IEKW is weaker: spectral energy of 60 day IEKW is ∼15% weaker (that is, sea level amplitude of IEKW is ∼10% weaker), that of 80 day IEKW ∼45% weaker (sea level ∼25% weaker) and that of 120 day IEKW ∼40%–45% weaker (sea level ∼25%–30% weaker). When excluding the January 1997 to June 1998 period, spectral energy of 80 day and 120 day IEKW are much closer to the observed (not shown). This indicates that the model reproduces well the amplitude of these waves, except during the 1997–98 El Niño when they were much stronger (Figure 4a). On the other hand, the energy of the 60 day IEKW did not show significant sensitivity to El Niño.

4.2. Poleward Propagating CTW

[38] As explained in section 2.3, EOFs of band-pass-filtered alongshore velocities are used to describe the cross-shore and alongshore structure of CTW. Rossby radii of deformation were computed from the model outputs in order to determine the width of the cross-shore sections used for

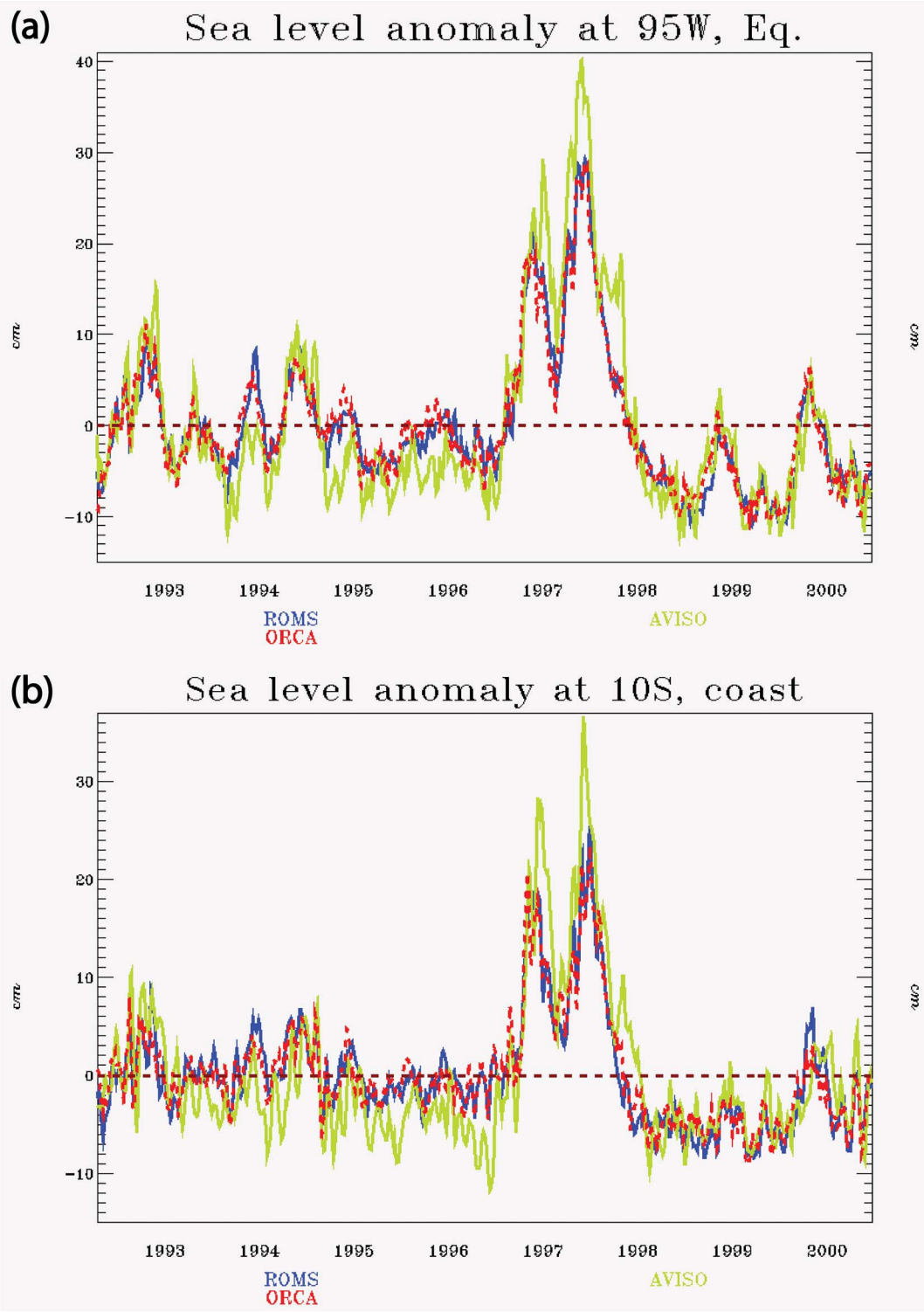

Figure 4. SLA (cm) simulated in R5d (solid blue line), in ORCA (dashed red line), and from AVISO data (solid green line) at (a) 0°N, 95°W and (b) 10°S, 78.3°W as a function of time. Units are cm.

the EOF calculation. Note however that results from the EOF analysis did not exhibit significant sensitivity to the width of the cross-shore section.

[39] At 5°S, the statistically dominant first mode for (50–70 days)$^{-1}$ frequencies, which explains 47% of the variance (Table 3), exhibits significant alongshore current variability trapped near the coast (Figure 6a). The velocity structure is baroclinic, dominated by the first vertical mode with a change of sign near 500–600 m depth (see also Figure 7), and decays seaward with a length scale of the order of the deformation radius (∼150 km in the model, consistently with *Chelton et al.* [1998]), similarly to the expected

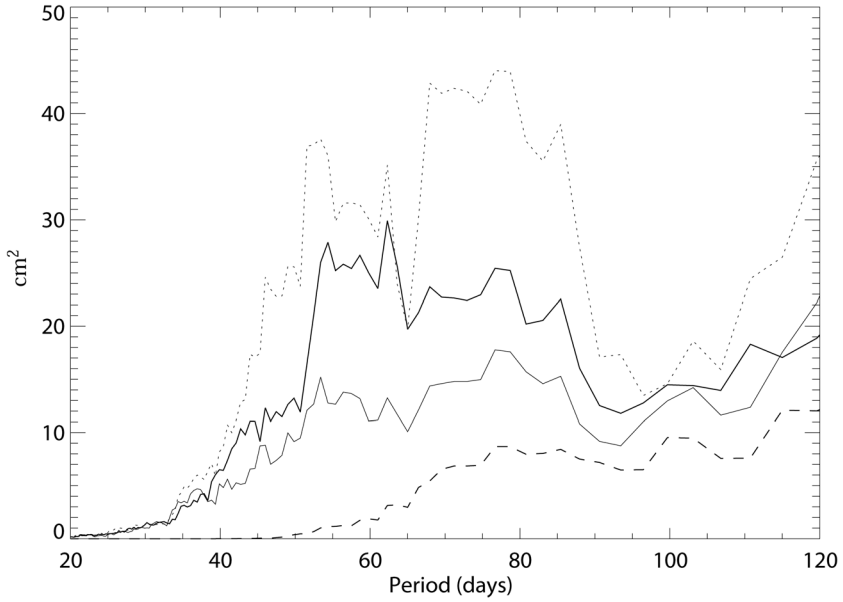

Figure 5. Frequency spectra for basin-wide (∼16,500 km) eastward propagations from high-pass-filtered SLA (f_c = 150 days) simulated by ORCA 5-daily (thick solid line) and monthly (thick dashed line) outputs, by SODA 5-daily outputs (thin solid line), and from AVISO data (thin dotted line) at the equator between 132°E and 80°W. Spectrum units are cm^2.

behavior of idealized coastal Kelvin waves (CKW) propagating along a vertical wall over a flat bottom [*Gill*, 1982]. Similar results were obtained between 10°S and 25°S (Figure 7). The magnitude of maximum variability ranges from 15 cm/s at 5°S (Figures 6a and 7) to 22 cm/s at 25°S (not shown), ∼2–3 times higher than the mean PCUC and of the order of the mean CPCC off Peru (Figure 1a). These results are consistent to a large extent with those obtained by *Clarke and Ahmed* [1999, Figure 14a] with a coastal wave propagation model including the effects of bottom topography and friction. They found similar coastally trapped structures, with maximum velocities near the coast and at or near the surface, decreasing with depth but with a slight increase at deeper layers, and with decreasing cross-shore scales away from the equator. Their maximum velocities are in the 12–16 cm/s range, i.e., slightly weaker than obtained here. This may be due to differences in the mean alongshore flow, as noted by *Shaffer et al.* [1997]. Note, however, that a direct quantitative comparison with the work by *Clarke and Ahmed* [1999] is made difficult by the differences in the latitudes chosen for the cross sections, and by the bottom topography and stratification profiles, which do not vary alongshore in their model.

[40] Lag correlation plots between PCs of the first EOF mode taken at different latitudes show a clear poleward propagation, especially between 5°S and 25°S (Figure 6b). The associated phase speed estimates were found to vary strongly with latitude (Table 4). There are several reasons for that. The most obvious is the large uncertainty associated with the estimated phase lag values because of the use of 5 day averages: for instance, maximum lag correlation was obtained for a 5 day lag at both 10°S and 15°S (Table 4), whereas in reality, it is likely obtained between these latitudes, say, around 12.5°S. The corresponding average phase speed is 228 km/d i.e., 2.64 m/s, which is equal to the estimated value at 20°S (Table 4). At 25°S, a maximum lag correlation of 0.45 is obtained for a phase lag of 20 days, yielding a rather slow phase speed of 143.5 km/d i.e., 1.66 m/s (Table 4). However, a correlation coefficient only slightly smaller (0.39) is obtained for a phase lag of 15 days: the phase speed corresponding to this latter estimate is 191.3 km/d i.e., 2.21 m/s, which is closer to the values obtained further North. Another factor that can influence the long-wave phase speed of CTW is shelf and slope bottom topography [*Clarke and Ahmed*, 1999, and references therein]: a steeper topography off Chile compared to Peru (Figures 2a, 2b, and 1) may cause the reduced phase speed south of 20°S.

[41] Regardless of alongshore variations, these estimated phase speeds are ∼10%–25% slower than the 2,89 ± 0.04 m/s observed by *Clarke and Ahmed* [1999]. The discrepancy may be due to a number of factors, such as the alongshore distance estimated from a smoothed coastline (black solid line on Figure 1 by *Clarke and Ahmed* [1999]), which underestimates the real length of the coastal

Table 3. Fractions of the (50–70 days)$^{-1}$ Band-Pass-Filtered Alongshore Current Variance (%) Explained by the First Three PCs From the EOF Analyses Performed in R5d at 5°S, 10°S, 15°S, 20°S, 25°S, 30°S, and 35°S[a]

Latitude (°S)	Mode 1	Mode 2	Mode 3
5	47	19	9
10	55	23	8
15	51	23	8
20	59	23	5
25	64	23	5
30	46	33	8
35	43	38	9

[a]See text. PC, principal component; EOF, empirical orthogonal function.

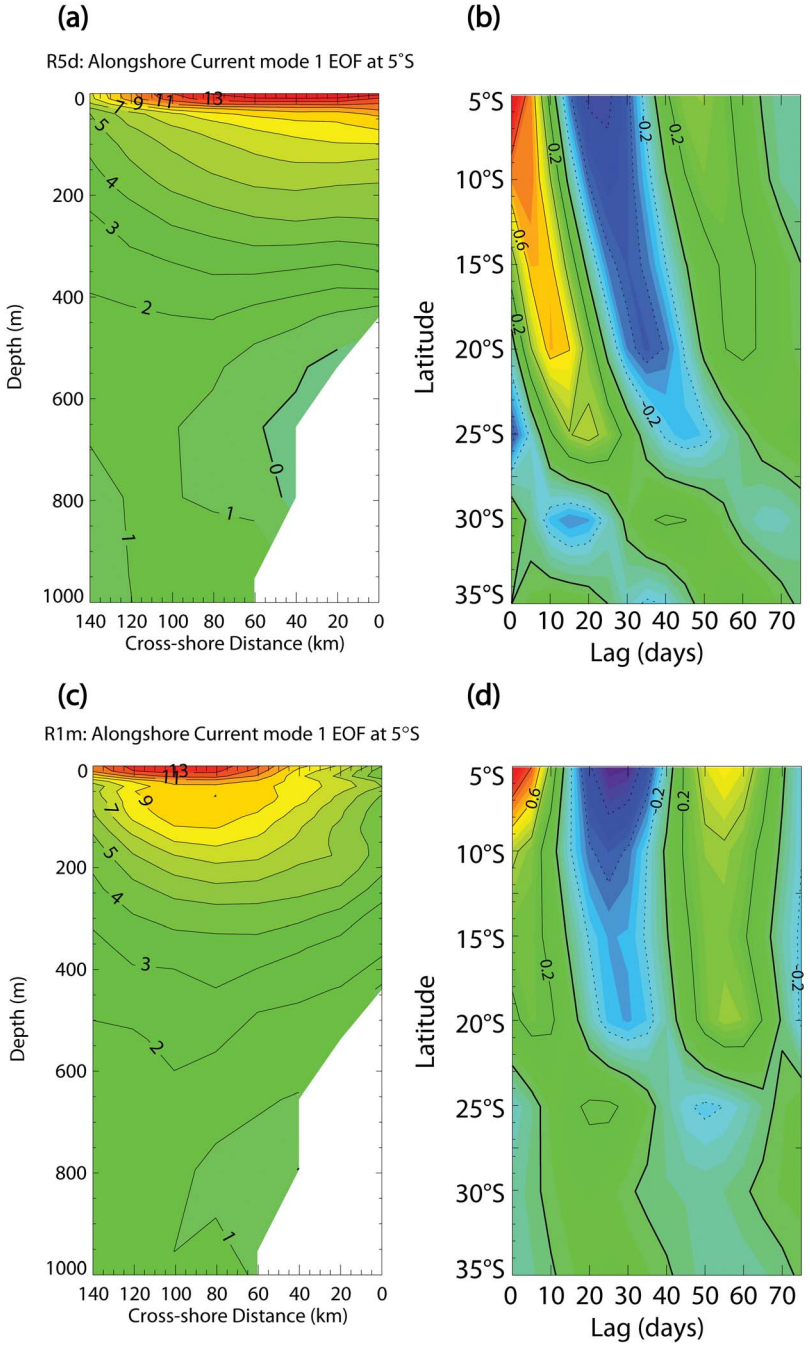

Figure 6. (a) First empirical orthogonal functions (EOF) mode spatial pattern of (50–70 days)$^{-1}$ band-pass-filtered alongshore current anomalies from R5d performed from the surface to the bottom over a cross-shore section at 5°S of length close to the first Rossby radius of deformation, as a function of seaward cross-shore distance (km) and depth (m). Units are cm/s and CI is 1 cm/s. (b) Lag correlation as a function of phase lag (days) and latitude (°) between the first EOF mode time series at 5°S and the first EOF mode time series at higher latitudes in R5d. Values are graphically interpolated from a 5° meridional grid. Values at 5°S are for the autocorrelation function. CI is 0.2, and dashed lines are for negative correlations. Only positive lags are plotted. (c and d) Same as Figures 6a and 6b, except for R1m.

waveguide and hence the modeled propagation speed. Another possibility is that compared to the real ocean, the model IEKW may have more energy in higher-order modes, which propagate slower. Also, *Clarke and Ahmed* [1999] defined the intraseasonal band as (30–70 days)$^{-1}$, whereas here we consider the slightly lower-frequency (50–70 days)$^{-1}$ band. As argued by these authors, a lower frequency enhances the dynamical importance of friction and thus reduces the phase speed, but also yields a higher critical latitude that increases the alongshore-averaged phase speed (infinite speeds are theoretically found equatorward of the critical latitude). Which of these opposing effects dominates

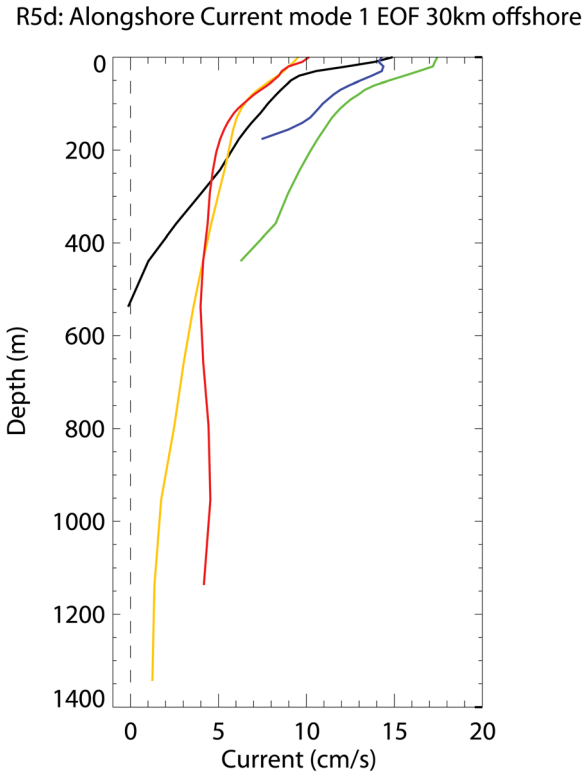

Figure 7. Same as Figure 6a, except at ~30 km offshore at 5°S (black), 10°S (blue), 15°S (green), 20°S (orange), and 25°S (red).

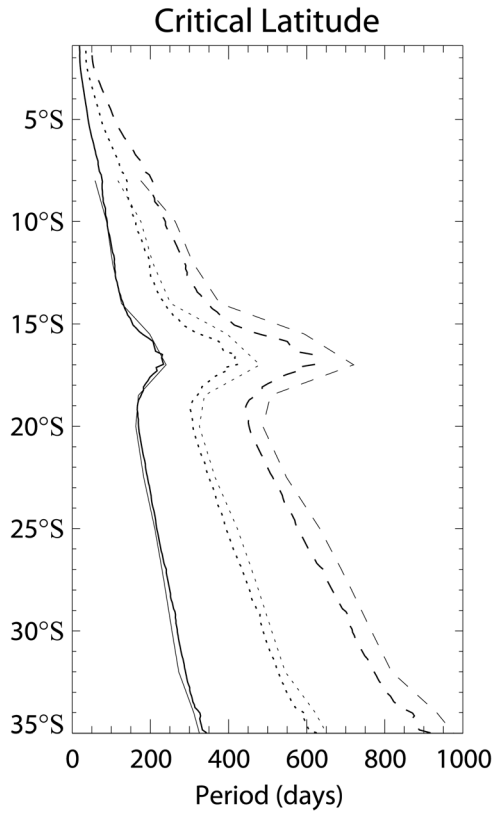

Figure 8. Critical latitude (degrees) as a function of frequency (days) for the first, second, and third baroclinic modes (solid, dotted, and dashed lines, respectively) for R5d and by *Clarke and Shi* [1991] (thick and thin lines, respectively). Phase speeds used for the computation of R5d critical latitudes were averaged along the 3000 m isobath from 5°S to 35°S (see text).

in this case is unclear. However, critical latitudes associated with the median frequency values $((50 \text{ days})^{-1}$ and $(60 \text{ days})^{-1}$, respectively) differ only by ~1° (see Figures 8 and 9), so the frictional effect may dominate and contribute to the slower phase speeds than observed.

[42] The model phase speed estimates are all faster than the first baroclinic mode phase speed over the continental slope at about 3500 m depth ($c_1 \sim 2.1$ m/s, see Table 5), which was derived from the vertical mode decomposition. This is consistent with increased speed due to realistic bottom topography, compared to the idealized CKW case assumed by the WKB method. Together with the first baroclinic mode-like vertical structure of the EOFs, it suggests that the first baroclinic mode dominates 60 day CKW/CTW propagation in this region. More generally, these results clearly demonstrate the presence between 5°S and 25°S of poleward propagating CTW with a 60 day periodicity in the R5d ROMS simulation, consistently with what is expected from linear theory and from the results of IEKW propagation analysis.

Table 4. Lag Correlation Analysis Between the First EOF Mode Time Series at 5°S and the First EOF Mode Time Series at Higher Latitudes in R5d: Maximum Lag Correlation and Associated Phase Lag, Distance From the Section at 5°S, and Estimated Phase Speed[a]

Latitude (°S)	Maximum Lag Correlation (%)	Lag (days)	Distance (km)	Phase Speed (km/d)	Phase Speed (m/s)
10	75	5	750	150	1.74
15	65	5	1530	306	3.54
20	66	10	2280	228	2.64
25	45	20	2870	143.5	1.66

[a]See Figure 6b. The distance was estimated from the smoothed coastline used by *Clarke and Ahmed* [1999] (black solid line on their Figure 1).

4.3. IEKW, RW, and the Critical Latitude

[43] As mentioned previously, the critical latitude linear theory (CS91) provides a theoretical background to understand the propagation/reflection of IEKW and generation of CTW in the tropical-to-subtropical eastern Pacific Ocean. Critical latitudes provided by CS91 were derived using the following formulation for a smooth nonmeridional boundary:

$$T_{c_n} = -\frac{4\pi R \tan\varphi}{c_n \sin\theta} \tag{4}$$

where T_{cn} (c_n) is the critical period (phase speed) of the wave for the nth baroclinic mode, R is the earth radius, φ is the critical latitude and θ is the coastline angle relatively to the east direction (see CS91 for details).

[44] To check the relevance of the CS91 critical latitudes for our model configuration, equation (4) was applied to estimates of coastline angle and baroclinic mode phase speeds as derived from model topography and mean stratification. Critical latitudes for phase speeds computed along

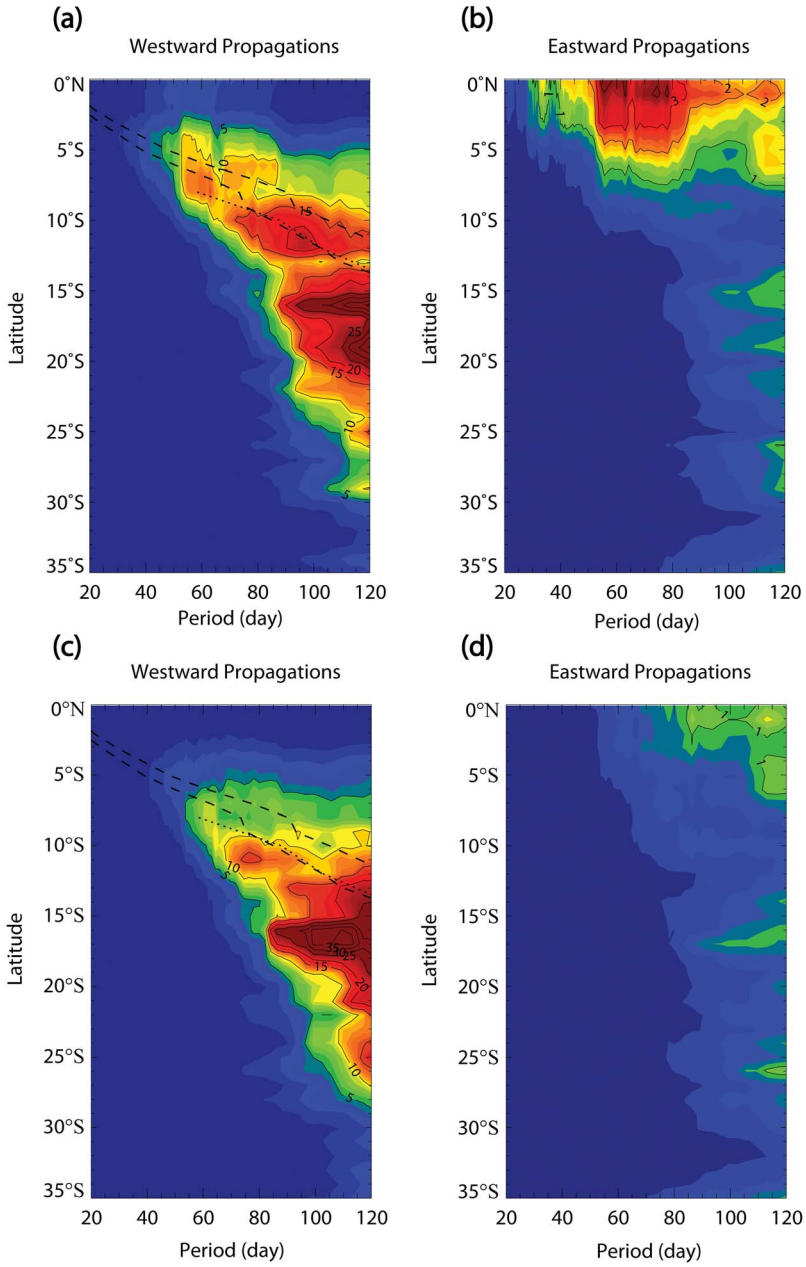

Figure 9. Time period spectra of the high-pass-filtered (f_c = 150 days) first baroclinic mode contribution to SLA simulated in R5d as a function of latitude for (a) westward and (b) eastward propagations. The plots were obtained from the results of frequency-wavelength decompositions performed along zonal sections every degree of latitude (see section 2.3) and integrated over the wavelength space (from k = 1 to k = 4). Units are cm^2. CI is 5 cm^2 (1 cm^2) for Figure 9a (Figure 9b). The top (bottom) dashed line on Figure 9a is the critical latitude derived from estimates of the first baroclinic mode phase speed computed along the 2000 m (3500 m) isobath. The dotted line is the estimate of *Clarke and Shi* [1991]. (c and d) Same as Figures 9a and 9b, except for R1m.

the 3000 m and 3500 m isobaths are in good agreement with CS91, though slightly further away from the equator for the second and third baroclinic modes (Figure 8). Note that these isobaths were chosen (1) because they are located along the steep continental slope and thus provide a framework comparable to some extent to the flat bottom vertical wall idealized case considered by CS91 and (2) since phase speeds for these isobaths (Table 5) are the closest to the ones estimated by *Chelton et al.* [1998] from climatological data.

[45] Results from the vertical mode decomposition are then used to characterize IEKW propagating eastward in the equatorial region, and RW propagating westward inside the regional model. Space-time analysis applied to baroclinic mode contributions to sea level anomalies allows describing

Table 5. Meridionally Averaged First to Third Baroclinic Mode Phase Speeds c_n in the 2° Coastal Band Along Different Isobaths for R5d

Depth (m)	c_1 (m/s)	c_2 (m/s)	c_3 (m/s)
2000	1.7	1.0	0.7
2500	1.9	1.0	0.7
3000	2.0	1.1	0.8
3500	2.1	1.2	0.8

equatorial Kelvin wave and planetary wave motion in the regional domain and their variations with latitude. Consistently with results from ORCA (Figure 5), IEKW are observed inside the regional model domain between about 0°N and 5°S, with frequencies around 60 days, 80 days and 120 days for the first baroclinic mode (Figure 9b).

[46] Westward propagation can also be evidenced (Figure 9a). Westward propagating features become more energetic than eastward propagating IEKW south of ~3°S–4°S, where equatorially trapped IEKW eventually vanish. As expected from linear theory, for frequencies and latitudes low enough, offshore westward propagation is observed, suggesting the presence of RW forced at the coast by CTW/CKW, whereas for frequencies and latitudes high enough, there is no significant wave propagation in the zonal direction. However, the associated critical latitudes/frequencies depart significantly from those derived from linear theory, especially for the lower frequencies, no matter which estimates of the critical latitude are considered (those from CS91 or those from model-derived parameters; see Figure 9a). Indeed, whereas linear theory does not expect any equatorially forced RW propagation south of 14°S in the $(90 \text{ to } 120 \text{ day})^{-1}$ frequency band, highly energetic westward motion is observed as far south as 30°S for the first baroclinic mode (Figure 9a). Similar results were obtained for the second and third baroclinic modes (not shown), but it was chosen to focus on the more energetic first mode.

5. Sensitivity of the Model Variability to the Remote Intraseasonal Forcing

[47] We have shown in the previous section that the simulation features baroclinic westward propagating intraseasonal variability in the inner basin south of the critical latitude. Two kinds of dynamical structures may be responsible for such variability: RW and mesoscale eddies, which are difficult to separate. To investigate the role of IEKW in the simulated westward propagations north and south of the critical latitude, results obtained from R5d were compared to those from R1m, in which 60–80 days harmonics are strongly damped (see 2.1).

5.1. Baroclinic Wave Propagation

[48] Frequency-wavelength decomposition applied to the ORCA monthly mean outputs shows that IEKW are damped at the western boundary of R1m (Figure 5, thick dashed line): frequencies higher than $(50 \text{ days})^{-1}$ are absent, spectral energy of 60 day IEKW has been divided by about a factor 10–15 (that is, sea level amplitude of IEKW has been divided by ~3–4) and that of 80 day IEKW by about 2.5 (sea level divided by ~1.5 i.e., reduced by ~35%). 120 day oscillations are the least damped among our frequencies of interest, energy of the spectral peak being divided by 1.5 (sea level divided by ~1.2 i.e., reduced by ~20%) compared to its 5-daily mean counterpart. Similar differences may be seen in the R5d and R1m IEKW (Figures 9b and 9d). Consistently with the IEKW damping, intraseasonal equatorial sea level variability at 95°W is reduced by ~45% in the ORCA monthly means (compared to the 5-daily means) and by ~35% in R1m (compared to R5d); see Table 2.

[49] Such damping of 50 to 80 day IEKW reduces the triggering of CTW propagation in R1m. Indeed, the EOF analysis (see section 4.2) performed with R1m reveals a different structure for the first EOF mode for $(50–70 \text{ days})^{-1}$ frequencies at 5°S compared to R5d (Figure 6c). The mode shows a surface-trapped maximum current variability, which is not coastally trapped as in R5d (Figure 6a), consistently with the damping of high-frequency IEKW in R1m. As for R5d, the first EOF mode was identified every 5° of latitude and the associated PCs were then lag correlated with that obtained at 5°S. The resulting figure (Figure 6d) does not exhibit a clear poleward propagation as for R5d (Figure 6b). The lag 0 correlation value at 10°S (15°S) is only ~0.4 (~0.2). In addition, the poleward propagation diagnosed from Figure 6 is inconsistent with a baroclinic CTW, since the associated phase speed is too high (greater than ~4.5 m/s). Furthermore, intraseasonal sea level variability near the coast of central Peru (10°S) is reduced by ~45% in R1m compared to R5d (Table 2), supporting the hypothesis that 60 day CTW in R5d are triggered by 60 day IEKW. We also verified that the higher-order EOF modes (modes 2–7) in R1m were not similar to the CTW mode identified in R5d.

[50] Westward propagations in R1m exhibit remarkable differences with those obtained from R5d (Figures 9a and 9c). In particular, 50 to 100 day westward propagating features equatorward of the critical latitude are ~40%–70% weaker in R1m (Figures 9a and 9c), which suggests that such westward propagations are the signature of equatorially forced propagating structures. On the other hand, westward propagating energy is found south of the critical latitude in both simulations with similar levels (Figures 9a and 9c). This confirms the presence of locally forced westward propagating RW and/or mesoscale eddies poleward of the critical latitude, independently of the presence of high-frequency equatorial forcing.

5.2. Eddy Activity

[51] To document further this hypothesis, differences between R5d and R1m in terms of eddy activity are examined. Figure 10a represents the difference in mean surface EKE between the two simulations (R5d minus R1m), using the ensemble experiments described in 2.1. As expected, annual mean surface EKE is significantly higher in R5d compared to R1m along most of Peru and Chile's coast, near the equator and off northern Peru (north of 8°S). In these areas, the difference is of the order of 10 $\text{cm}^2\ \text{s}^{-2}$ i.e., 10%, and up to ~50% in the very nearshore off northern Peru. At some particular locations of the coastal region there is no EKE increase (near 13°S–14°S, ~20°S and south of 28°S). Such pattern and its meridional gradient (higher EKE closer to the equator) suggest that the EKE increase is likely due to the passing IEKW, RW, and CTW. On the other hand, EKE is almost unchanged in the offshore region. Two patches of

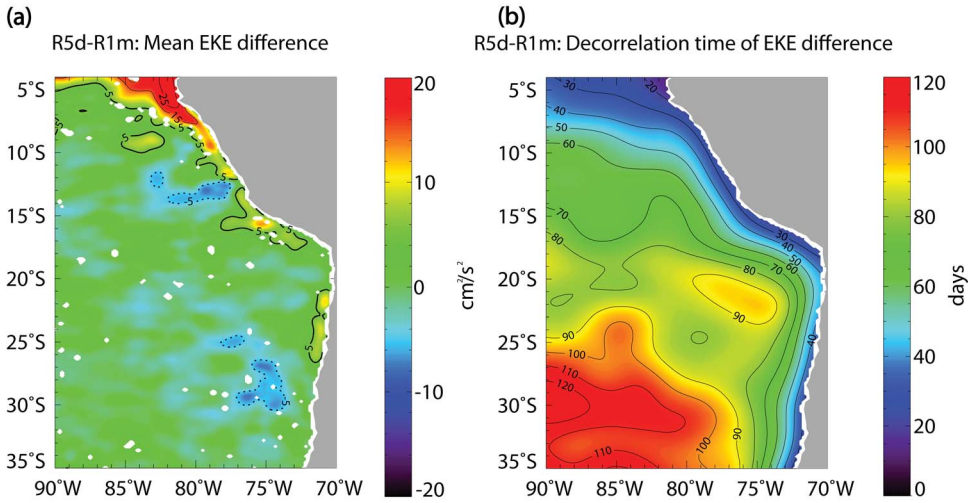

Figure 10. (a) Difference between ensemble mean EKE computed from SLA simulated in R5d (10 members) and that simulated in R1m (10 members). Only the values significant at the 95% level are shown. Units are cm^2/s^2. CI is 10 cm^2/s^2. (b) Decorrelation time (days) used for the computation of significance levels in Figure 10a (see text). CI is 10 days. The data in Figure 10a (Figure 10b) have been smoothened using five passes of a 1/3° × 1/3° (2° × 2°) low-pass filter.

statistically significant EKE reduction were found off central Peru (∼12°S–14°S) and central Chile (∼26°S–30°S), but their amplitude is weak (∼5 $cm^2\ s^{-2}$ i.e., 5%–10%) and their spatial extent is reduced (of the order of the deformation radius for the Peru patch). These results suggest that 60 day intraseasonal CTW have a relatively moderate (weak) effect on EKE near the coast (offshore).

5.3. Baroclinic Instability and Other Energy Sources

[52] In the following, an energy budget is performed in a 100 m surface layer for both R5d and R1m. It is aimed at explaining the source and sink terms of change in EKE associated with IEKW activity (see 2.3). Figure 11 presents ensemble mean energy fluxes F_eK_e, K_mK_e, and P_eK_e for both simulations, alongshore-averaged off northern Peru between 6°S and 8°S (where EKE increases both nearshore and offshore) and off central Peru between 13°S and 14°S (where EKE weakly increases nearshore and slightly decreases offshore), as a function of westward distance from the coast. In both regions, energy transfer terms are highest just off the coast (at a distance of ∼50–100 km) and decay in the offshore direction. Energy flux due to baroclinic instability dominates the EKE budget, with peak values of 0.5 and 1.2 $cm^3\ s^{-3}$ off northern Peru (6°S–8°S) and central Peru (13°S–14°S), respectively, accounting for ∼60%–65% of the maximum total energy fluxes (Figure 11). Barotropic instability and wind work transfer terms are of second order, each accounting for ∼20% of the total.

[53] The term that experiences the largest differences between R5d and R1m is the baroclinic instability term, which is such that differences in total energy conversion closely follow the ones in baroclinic instability (Figures 11a and 11b). Off the northern coast, a ∼0.1–0.2 $cm^3\ s^{-3}$ decrease in R1m (∼35% near 150 km offshore) is observed 100–200 km offshore (Figure 11a). In contrast, between 13°S and 14°S there is a ∼0.3 $cm^3\ s^{-3}$ increase in R1m (∼40% near 110 km offshore) from ∼70 to 150 km offshore (Figure 11b). Note that the K_mK_e flux difference has a nonnegligible contribution (∼40%) to the total difference in the latter region. In both regions, there are almost no differences in the sum of the conversion terms between R5d and R1m in the first 70 km nearshore.

[54] The offshore changes in energy conversion explain to some extent the offshore EKE changes (Figure 10a). Indeed, north of 8°S the offshore increase in EKE production is important, resulting in a clear increase in EKE in R5d. Off central Peru (13°S–14°S), the slight offshore EKE reduction is consistent with the P_eK_e and K_mK_e reduction from 70 to 150 km offshore. The structures of the mean alongshore current and its vertical shear in R1m and R5d were compared, and almost no differences were found (not shown). Thus P_eK_e differences cannot be simply related to baroclinic instability through changes in the current vertical shear, and may rather be explained by changes in RW activity (see Figures 9a and 9c).

[55] Interestingly, the nearshore EKE increase cannot be explained by the negligible changes in the sum of energy conversion terms (Figure 11b, thick lines), but is rather interpreted as equatorially generated CTW activity. The latter is consistent with the much weaker coastal increase in EKE south of 10°S, in agreement with a poleward dissipation of CTW (Figure 6b) [*Clarke and Ahmed*, 1999] and the scattering of energetic CTW into westward propagating RW [e.g., *Milliff and McWilliams*, 1994].

6. Sensitivity to the OGCM Boundary Forcing

[56] The sensitivity of the changes in eddy activity to the IEKW amplitude is investigated by using another OGCM as open boundary forcing in order to verify the robustness of our results. This leads to a regional solution with different levels of IEKW and EKE. Here we chose to use 5-daily

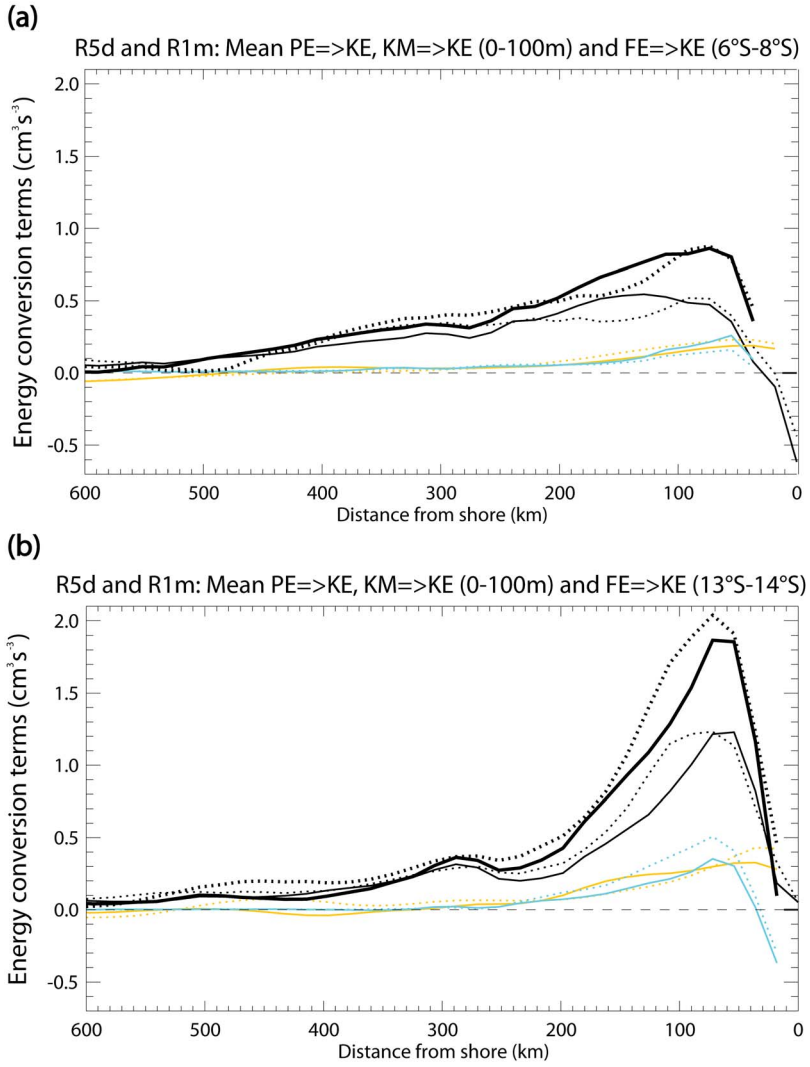

Figure 11. Annual ensemble mean (10 members) P_eK_e (thin black line), K_mK_e (thin blue line), F_eK_e (thin orange line), and their sum (thick black line) in the first 100 m depth, alongshore-averaged between (a) 6°S and 8°S and (b) 13°S and 14°S, as a function of westward distance from the coast (km) in R5d (solid lines) and R1m (dashed lines). Units are cm^3 s^{-3}.

outputs of the SODA OGCM. Compared to the solution forced by ORCA (R5d), the solution forced by SODA (R5d-SODA) displays a more intense EUC, PCUC, and CPCC (not shown) [see also *Echevin et al.*, 2011] and tends to overestimate the mean EKE compared to AVISO data, especially off Peru (Figures 3b and 3c). Compared to R5d (Figure 3a), the EKE pattern in R5d-SODA is very similar, but the amplitude is ∼40% higher.

[57] On the other hand, IEKW are weaker in SODA compared to ORCA, as seen in the basin-wide sea level frequency-wavelength decomposition (Figure 5): amplitudes of 60 day and 80 day IEKW are ∼30% and ∼15%–20% weaker, respectively. Note that this corresponds to amplitudes ∼35%–40% weaker than in AVISO data. Importantly, the dominant IEKW frequencies seen in AVISO and ORCA data are also found in SODA.

[58] On the basis of the results previously found with ORCA OBC, weaker IEKW in the SODA forcing compared to ORCA forcing are expected to lead to a weaker nearshore increase in EKE, assuming (1) a linear response of EKE changes to IEKW amplitude and (2) that the background mean state and EKE level do not play a major role in the CTW-eddy interaction. To verify this hypothesis, we repeated the procedure consisting in forcing ROMS with monthly SODA outputs (R1m-SODA simulation). Figure 12 is the same as Figure 10a, but for SODA OBC. It shows that although EKE levels are higher with SODA forcing (Figures 3a and 3b), the impact of IEKW on EKE is weaker. Indeed, the EKE difference pattern in Figure 12 resembles that in Figure 10a, but with a weaker amplitude along the coast. Offshore patterns also present similarities with an intensification north of 10°S and a slight decrease around ∼13°S–14°S. The former has a larger amplitude and extends further offshore for SODA OBC than for ORCA OBC, whereas the latter is weaker and more localized in SODA OBC.

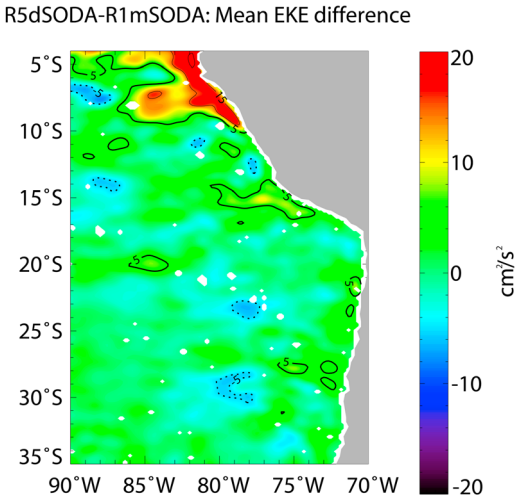

Figure 12. Same as Figure 10a, except for R5d-SODA and R1m-SODA.

[59] Overall, EKE is practically unchanged in the offshore region (south of 10°S), which confirms that the IEKW effects are weak outside of a narrow coastal band.

7. Discussion and Conclusions

[60] A regional eddy-resolving ocean model with boundary conditions and atmospheric forcing from the 1992–2000 period is used to study the influence of intraseasonal equatorial Kelvin waves (IEKW) with frequencies higher than $(120\ \text{days})^{-1}$ on mesoscale eddy activity off the western coast of South America. The focus is on 50 to 80 day Kelvin waves.

[61] The model is shown to reproduce most characteristics of the mean circulation in this region, including a surface equatorward coastal jet, a subsurface poleward undercurrent, coastal upwelling, and the observed pattern of eddy kinetic energy (EKE) that features local maxima near the coast of Peru and in the coastal transition zone off central Chile. A stronger coastal jet and weaker undercurrent than observed may be due to weak nearshore curl in the ERS wind forcing or to biases in the ORCA model used as open boundary conditions (OBC). However, such biases probably do not greatly affect the processes of interest for this study: baroclinic instability and coastal trapped wave (CTW) propagation (see below). The simulated EKE in the equatorial region is found to be weaker than observed, but our results suggest that such discrepancy is not critical for our study. The model also exhibits similar levels of sea level variability compared to altimetric data, including for intraseasonal frequencies, though with a weaker amplitude, which is partly attributed to an underestimation of the strong IEKW during the 1997–98 El Niño.

[62] The IEKW forcing is then assessed in the ocean general circulation model (OGCM) forcing the regional model, and exhibits energy peaks at 60 and 80 days, consistently with observations. A vertical mode decomposition of the regional model variability allows its interpretation in terms of IEKW and intraseasonal Rossby waves (RW).

[63] In agreement with linear theory, it is shown that incoming 50 to 80 day IEKW are responsible for both the poleward propagation of 60 day CTW along the coasts of Peru and northern Chile and the westward propagation of 50 to 100 day RW equatorward of the theoretical critical latitude, which ranges from 6°S to 12°S for the first baroclinic mode.

[64] The analysis also reveals highly energetic westward propagation at intraseasonal frequencies poleward of the critical latitude. Such propagation is shown to be present in the model solution even in the absence of 50 to 80 day IEKW at the open boundaries, suggesting a local rather than a remote intraseasonal equatorial forcing. The simulation with IEKW forcing is associated with a clear increase (∼50% near 5°S) in EKE near the equator and a moderate increase (∼10%) in a narrow band along the coast. This suggests that IEKW-induced CTW enhance EKE near the coast but have a weak impact on the ocean interior. Quantifying the fraction of EKE changes due to CTW instead of RW and mesoscale eddies would require the use of simple CTW models [e.g., *Brink*, 1982; *Chapman*, 1987; *Clarke and Ahmed*, 1999; *Jordi et al.*, 2005], which represents a significant amount of work when repeated over the ensemble simulations. This is beyond the scope of this study and is left for future work.

[65] A simplified EKE budget provides insight on the mechanisms responsible for the EKE changes due to CTW activity. It is shown that the increase in mean nearshore EKE off northern and central Peru between a simulation with 5-daily mean OBC and monthly mean OBC is not associated with a nearshore increase in baroclinic instability. This suggests that the EKE increase may be the signature of the fluctuating alongshore currents associated with the poleward propagating waves.

[66] Few studies have extensively addressed the question of the influence of CTW on eddy activity in eastern boundary current regions. *Zamudio et al.* [2001, 2006, 2007] in the northeastern Pacific (12°N–24°N) and *Melsom et al.* [1999] in the Gulf of Alaska (46°N–60°N) invoke instabilities of the coastal currents as the mechanisms by which CTW can impact the generation of mesoscale eddies. They found that downwelling CTW can generate and/or strengthen anticyclonic eddies by accelerating the dominant poleward surface coastal current in these regions. Similar effects on the poleward undercurrent in the Peru-Chile region have also been shown during ENSO events [*Colas et al.*, 2008; *Montes et al.*, 2011]. The reinforced jet is associated with strong vertical and horizontal shears, which favor the development of baroclinic and barotropic instabilities. However, we show in this study that the average effect (over a long period such as 1992–2000) of successive upwelling and downwelling CTW on the eddy activity is weak, as shown by the moderate EKE changes evidenced offshore of a ∼100 km coastal band.

[67] The robustness of the IEKW impact on EKE is assessed by comparing the model solution to a solution with a boundary forcing derived from a different OGCM. Although the latter features a ∼40% higher EKE compared to the original solution, the pattern of EKE changes (a moderate increase along the equatorial-coastal waveguide) appears only slightly sensitive to such increase in background levels. The solution with different OBC is

shown to exhibit weaker nearshore EKE increase, consistently with a weaker IEKW forcing the regional model.

[68] Another factor likely to influence our results is the model horizontal resolution. An increased resolution may allow better resolution of mesoscale processes contributing to the eddy activity. It may also lead to a better representation of the CTW cross-shore structure because of more realistic bottom topography. *Colas et al.* [2012] using a higher-resolution (7.5 km) ROMS configuration of the Peru-Chile region found similar differences in EKE (nearshore increase north of 10°S, and weak, very localized offshore changes) between simulations forced with 5-daily and monthly OBC (using SODA data over 2000–2006). This suggests that the 1/6° model used in this study may reasonably represent the IEKW effects on EKE.

[69] This may be explained in terms of the ratio between typical length scales of mesoscale structures for the region and horizontal resolution: the deformation radius varies from ∼200 km at the equator to ∼30 km at 35°S [*Chelton et al.*, 1998]. On the other hand, a 1/6° resolution corresponds to ∼18.5 km at the equator and ∼15.2 km at 35°S. Hence, typical mesoscale structures can be represented with ∼10 grid points off Peru in our model. Smaller values for this ratio where found to be sufficient to study the effect of CTW on mesoscale eddies off the coast of Mexico [*Zamudio et al.*, 2007]. On the other hand, mesoscale eddies off central Chile are represented with only ∼2 grid points, which may not be sufficient to fully resolve them. Nevertheless, our focus here is not on the central Chile region.

[70] On the other hand, recent work has argued that the length scale to consider is not the eddy length scale but the energy injection scale [*Tulloch et al.*, 2011]. In the HCS, it is less than half the deformation radius [*Tulloch et al.*, 2011, Figures 6a, A2a, and A2c]. Yet, these estimates are for the offshore region, as computations are based on global ocean climatologies that lack data from the coastal areas. In EBUSs, coastal upwelling controls the intensity of upwelling fronts and thereby the building of available potential energy used by baroclinic instability to generate mesoscale eddies. Hence, one may argue that the relevant scale is that of coastal Ekman divergence, which is roughly the length of the frictional boundary layer resulting from the overlapping of the surface and bottom Ekman layers in the shallow nearshore zone [*Estrade et al.*, 2008; *Marchesiello and Estrade*, 2010]. Rather than latitude, this scale is influenced by factors such as bottom topography and stratification, and is ∼5 km in the HCS: such a narrow layer is ensured by the steep continental slope off Chile [*Estrade et al.*, 2008] and by thin Ekman layers due to shallow stratification off Peru [*Marchesiello and Estrade*, 2010]. As discussed by *Renault et al.* [2012] and by *Marchesiello and Estrade* [2010], the model resolution is too coarse to represent it, thus upwelling takes place over one grid cell only. This limitation is common for most models of the current generation that do not have a resolution higher than 5 km [e.g., *Colas et al.*, 2012]. That said, the relative realism of the simulated mesoscale activity gives us confidence in our results.

[71] Note that the impact of IEKW on nearshore eddy activity in the Humboldt Current is likely larger in the real ocean than in our model experiments. Indeed, the regional model was found to underestimate the observed intraseasonal sea level variability by ∼40% (see Table 2), which is due to a large extent to weak IEKW in the OGCMs (∼10%–25% weaker than observed, see Figure 5), particularly during El Niño. The fact that a weaker IEKW forcing in SODA compared to ORCA induces weaker EKE changes (see section 6) suggests that with larger IEKW amplitude (i.e., more realistic), the increase in mean nearshore EKE may be higher than the ∼5–25 cm^2/s^2 simulated here (assuming a linear response of EKE changes to IEKW amplitude). A way to confirm this hypothesis would be to select a more realistic OGCM as OBC in order to force more energetic IEKW into the regional model. However, this is beyond the scope of the present study and will be reserved for future investigations.

[72] Our results may have implications for the understanding of the long-term evolution of the HCS considering that the IEKW has a low-frequency decadal modulation [*Dewitte et al.*, 2008b] and that IEKW activity may be modified in the eastern Pacific in a warmer climate because of increased occurrence of westerly wind bursts east of the date line [*Seiki et al.*, 2011]. How this climate variability may regulate nearshore turbulent activity in the HCS through IEKW intensity modulation needs further investigation based on long-term regional simulation. This is left for future work.

[73] At this stage, it is interesting to note that *Echevin et al.* [2012] found a ∼30% offshore EKE increase but no coastal increase off Peru in a quadrupling CO_2 climate scenario using monthly boundary conditions for ROMS, hence not taking into account a large fraction of IEKW forcing. Thus based on our results, we can speculate that nearshore EKE may be higher than that projected by *Echevin et al.* [2012], which could have a great impact on the functioning of the coastal ecosystem.

[74] **Acknowledgments.** The altimeter products were produced by SSALTO-DUACS and distributed by AVISO with support from CNES. CARS data were produced by the CSIRO Marine Laboratories. We are grateful to F. Ascani, J. Boucharel, A. Chaigneau, F. Codron, and D. Correa for fruitful discussions, to C. Ethée and G. Madec from LOCEAN/IPSL for making the ORCA05 simulations available, and to B. Giese from Texas A&M University for the SODA data. We also thank A. Albert and C. Hourdin from LOCEAN/IPSL and G. Cambon from LEGOS for their help with running the model simulations. The latter were performed on a PC cluster supported by the IRD/DSF "Spirales" project and on Brodie, the NEC SX8 computer at IDRIS (France). We are thankful to three anonymous reviewers, whose help allowed us to greatly improve the original manuscript. A. Belmadani was supported by IRD/DSF and by the ANR Peru Chile Climate Change (PCCC) and Peru Ecosystem Projection Scenarios (PEPS, VMCS-2008) projects. Additional support was provided by the Japan Agency for Marine-Earth Science and Technology (JAMSTEC), by NASA through grant NNX07AG53G, and by NOAA through grant NA17RJ1230 through their sponsorship of research activities at the International Pacific Research Center. B. Dewitte and V. Echevin are supported by IRD. F. Colas was supported by ANR PEPS. This is IPRC/SOEST publication 861/8573.

References

Adler, R. F., et al. (2003), The Version-2 Global Precipitation Climatology Project (GPCP) monthly precipitation analysis (1979–present), *J. Hydrometeorol.*, *4*, 1147–1167, doi:10.1175/1525-7541(2003)004<1147:TVGPCP>2.0.CO;2.

Albert, A., V. Echevin, M. Lévy, and O. Aumont (2010), Impact of nearshore wind stress curl on coastal circulation and primary productivity in the Peru upwelling system, *J. Geophys. Res.*, *115*, C12033, doi:10.1029/2010JC006569.

Belmadani, A. (2010), Impact of climate change in the Humboldt Current System simulated by a regional ocean model, Ph.D. thesis, Univ. Paul Sabatier, Toulouse, France. [Available at http://thesesups.ups-tlse.fr/777/.]

Bentamy, A., Y. Quilfen, F. Gohin, N. Grima, M. Lenaour, and J. Servain (1996), Determination and validation of average wind fields from ERS-1 scatterometer measurements, *Global Atmos. Ocean Syst.*, *4*, 1–29.

Bertrand, S., B. Dewitte, J. Tam, A. Bertrand, and E. Diaz (2008), Impacts of Kelvin wave forcing in the Peru Humboldt Current system: Scenarios of spatial reorganization from physics to fishers, *Prog. Oceanogr.*, *79*, 278–289, doi:10.1016/j.pocean.2008.10.017.

Blanco, J. L., A. C. Thomas, M.-E. Carr, and P. T. Strub (2001), Seasonal climatology of hydrographic conditions in the upwelling region off northern Chile, *J. Geophys. Res.*, *106*(C6), 11,451–11,467, doi:10.1029/2000JC000540.

Blanco, J. L., M.-E. Carr, A. C. Thomas, and P. T. Strub (2002), Hydrographic conditions off northern Chile during the 1996–1998 La Niña and El Niño events, *J. Geophys. Res.*, *107*(C3), 3017, doi:10.1029/2001JC001002.

Bouffard, J., L. Roblou, F. Birol, A. Pascual, L. Fenoglio-Marc, M. Cancet, R. Morrow, and Y. Ménard (2011), Introduction and assessment of improved coastal altimetry strategies: Case-study over the north western Mediterranean Sea, in *Coastal Altimetry*, edited by S. Vignudelli et al., chap. 12, pp. 297–330, Springer, Berlin, doi:10.1007/978-3-642-12796-0_12.

Boyer, T. P., et al. (2002), *World Ocean Database 2001*, vol. 2, *Temporal Distribution of Bathythermograph Profiles, NOAA Atlas NESDIS*, vol. 43, NOAA, Silver Spring, Md.

Brink, K. H. (1982), A comparison of long coastal trapped wave theory with observations off Peru, *J. Phys. Oceanogr.*, *12*, 897–913, doi:10.1175/1520-0485(1982)012<0897:ACOLCT>2.0.CO;2.

Camayo, R., and E. J. D. Campos (2006), Application of wavelet transform in the study of coastal trapped waves off the west coast of South America, *Geophys. Res. Lett.*, *33*, L22601, doi:10.1029/2006GL026395.

Capet, X., F. Colas, P. Penven, P. Marchesiello, and J. C. McWilliams (2008), Eddies in eastern-boundary subtropical upwelling systems, in *Oceanic Modeling in an Eddying Regime*, *Geophys. Monogr. Ser.*, vol. 177, edited by M. W. Hecht and H. H. Hasumi, pp. 131–147, AGU, Washington, D. C., doi:10.1029/177GM10.

Carton, J. A., and B. S. Giese (2008), A reanalysis of ocean climate using Simple Ocean Data Assimilation (SODA), *Mon. Weather Rev.*, *136*, 2999–3017, doi:10.1175/2007MWR1978.1.

Chaigneau, A., and O. Pizarro (2005), Eddy characteristics in the eastern South Pacific, *J. Geophys. Res.*, *110*, C06005, doi:10.1029/2004JC002815.

Chaigneau, A., A. Gizolme, and C. Grados (2008), Mesoscale eddies off Peru in altimeter records: Identification algorithms and eddy spatio-temporal patterns, *Prog. Oceanogr.*, *79*, 106–119, doi:10.1016/j.pocean.2008.10.013.

Chapman, D. C. (1987), Application of wind-forced, long, coastal-trapped wave theory along the California coast, *J. Geophys. Res.*, *92*, 1798–1816, doi:10.1029/JC092iC02p01798.

Chavez, F. P. (1995), A comparison of ship and satellite chlorophyll from California and Peru, *J. Geophys. Res.*, *100*, 24,855–24,862, doi:10.1029/95JC02738.

Chavez, F. P., A. Bertrand, R. Guevara-Carrasco, P. Soler, and J. Csirke (2008), The northern Humboldt Current System: Brief history, present status and a view towards the future, *Prog. Oceanogr.*, *79*, 95–105, doi:10.1016/j.pocean.2008.10.012.

Chelton, D. B., R. A. deSzoeke, M. G. Schlax, K. El Naggar, and N. Siwertz (1998), Geographical variability of the first baroclinic Rossby radius of deformation, *J. Phys. Oceanogr.*, *28*, 433–460, doi:10.1175/1520-0485(1998)028<0433:GVOTFB>2.0.CO;2.

Clarke, A. J. (1983), The reflection of equatorial waves from oceanic boundaries, *J. Phys. Oceanogr.*, *13*, 1193–1207, doi:10.1175/1520-0485(1983)013<1193:TROEWF>2.0.CO;2.

Clarke, A. J., and R. Ahmed (1999), Dynamics of remotely forced intraseasonal oscillations off the western coast of South America, *J. Phys. Oceanogr.*, *29*, 240–258, doi:10.1175/1520-0485(1999)029<0240:DORFIO>2.0.CO;2.

Clarke, A. J., and C. Shi (1991), Critical frequencies at ocean boundaries, *J. Geophys. Res.*, *96*, 10,731–10,738, doi:10.1029/91JC00933.

Colas, F., X. Capet, J. C. McWilliams, and A. Shchepetkin (2008), 1997–98 El Niño off Peru: A numerical study, *Prog. Oceanogr.*, *79*, 138–155, doi:10.1016/j.pocean.2008.10.015.

Colas, F., J. C. McWilliams, X. Capet, and J. Kurian (2012), Heat balance and eddies in the Peru-Chile current system, *Clim. Dyn.*, doi:10.1007/s00382-011-1170-6, in press.

Cravatte, S., J. Picaut, and G. Eldin (2003), First and second baroclinic Kelvin modes in the equatorial Pacific at intraseasonal timescales, *J. Geophys. Res.*, *108*(C8), 3266, doi:10.1029/2002JC001511.

Croquette, M., G. Eldin, C. Grados, and M. Tamayo (2007), On differences in satellite wind products and their effects in estimating coastal upwelling processes in the south-east Pacific, *Geophys. Res. Lett.*, *34*, L11608, doi:10.1029/2006GL027538.

Da Silva, A. M., C. C. Young, and S. Levitus (1994), *Atlas of Surface Marine Data 1994*, vol. 1, *Algorithms and Procedures, NOAA Atlas NESDIS*, vol. 6, NOAA, Silver Spring, Md.

Dewitte, B., S. Illig, L. Parent, Y. duPenhoat, L. Gourdeau, and J. Verron (2003), Tropical Pacific baroclinic mode contribution and associated long waves for the 1994–1999 period from an assimilation experiment with altimetric data, *J. Geophys. Res.*, *108*(C4), 3121, doi:10.1029/2002JC001362.

Dewitte, B., M. Ramos, V. Echevin, O. Pizarro, and Y. duPenhoat (2008a), Vertical structure variability in a seasonal simulation of a medium-resolution regional model of the eastern South Pacific, *Prog. Oceanogr.*, *79*, 120–137, doi:10.1016/j.pocean.2008.10.014.

Dewitte, B., S. Purca, S. Illig, L. Renault, and B. S. Giese (2008b), Low-frequency modulation of intraseasonal equatorial Kelvin wave activity in the Pacific from SODA: 1958–2001, *J. Clim.*, *21*, 6060–6069, doi:10.1175/2008JCLI2277.1.

Dewitte, B., S. Illig, L. Renault, K. Goubanova, K. Takahashi, D. Gushchina, K. Mosquera, and S. Purca (2011), Modes of covariability between sea surface temperature and wind stress intraseasonal anomalies along the coast of Peru from satellite observations (2000–2008), *J. Geophys. Res.*, *116*, C04028, doi:10.1029/2010JC006495.

Dunn, J. R., and K. R. Ridgway (2002), Mapping ocean properties in regions of complex topography, *Deep Sea Res., Part I*, *49*(3), 591–604, doi:10.1016/S0967-0637(01)00069-3.

Echevin, V., F. Colas, A. Chaigneau, and P. Penven (2011), Sensitivity of the Northern Humboldt Current System nearshore modeled circulation to initial and boundary conditions, *J. Geophys. Res.*, *116*, C07002, doi:10.1029/2010JC006684.

Echevin, V., K. Goubanova, A. Belmadani, and B. Dewitte (2012), Sensitivity of the Humboldt Current system to global warming: A downscaling experiment of the IPSL-CM4 model, *Clim. Dyn.*, *38*(3–4), 761–774, doi:10.1007/s00382-011-1085-2.

Efron, B., and R. J. Tibshirani (1994), *An Introduction to the Bootstrap*, *Monogr. Stat. Appl. Probab. Ser.*, vol. 57, Chapman and Hall, Boca Raton, Fla.

Enfield, D. B. (1987), The intraseasonal oscillation in eastern Pacific sea levels: How is it forced?, *J. Phys. Oceanogr.*, *17*, 1860–1876, doi:10.1175/1520-0485(1987)017<1860:TIOIEP>2.0.CO;2.

Estrade, P., P. Marchesiello, A. Colin De Verdière, and C. Roy (2008), Cross-shelf structure of coastal upwelling: A two-dimensional extension of Ekman's theory and a mechanism for inner shelf upwelling shut down, *J. Mar. Res.*, *66*, 589–616, doi:10.1357/002224008787536790.

Food and Agriculture Organization (2009), The state of world fisheries and aquaculture 2008, report, Fish. and Aquacult. Dep., Rome.

Gill, A. E. (1982), *Atmosphere-Ocean Dynamics*, *Int. Geophys. Ser.*, vol. 30, edited by W. L. Donn, Academic, San Diego, Calif.

Grimshaw, R., and J. S. Allen (1988), Low-frequency baroclinic waves off coastal boundaries, *J. Phys. Oceanogr.*, *18*, 1124–1143, doi:10.1175/1520-0485(1988)018<1124:LFBWOC>2.0.CO;2.

Hayashi, Y. (1979), A generalized method of resolving transient disturbances into standing and traveling waves by space-time spectral analysis, *J. Atmos. Sci.*, *36*, 1017–1029.

Hayashi, Y. (1982), Space-time spectral analysis and its applications to atmospheric waves, *J. Meteorol. Soc. Jpn.*, *60*, 156–171.

Hormazabal, S., G. Shaffer, and O. Pizarro (2002), Tropical Pacific control of intraseasonal oscillations off Chile by way of oceanic and atmospheric pathways, *Geophys. Res. Lett.*, *29*(6), 1081, doi:10.1029/2001GL013481.

Hormazabal, S., G. Shaffer, N. Silva, and E. Navarro (2006), The Peru Chile undercurrent and the oxygen minimum zone variability off central Chile, *Gayana*, *70*, suppl. 1, 37–45.

Huyer, A., M. Knoll, T. Paluzkiewicz, and R. L. Smith (1991), The Peru undercurrent: A study in variability, *Deep Sea Res.*, *39*, 247–279.

Jiang, C., L. Thompson, K. A. Kelly, and M. F. Cronin (2009), The roles of intraseasonal Kelvin waves and tropical instability waves in SST variability along the equatorial Pacific in an isopycnal ocean model, *J. Clim.*, *22*, 3470–3487, doi:10.1175/2009JCLI2767.1.

Jordi, A., A. Orfila, G. Basterretxea, and J. Tintoré (2005), Coastal trapped waves in the northwestern Mediterranean, *Cont. Shelf Res.*, *25*, 185–196, doi:10.1016/j.csr.2004.09.012.

Kalnay, E., et al. (1996), The NCEP/NCAR 40-year reanalysis project, *Bull. Am. Meteorol. Soc.*, *74*, 789–799.

Kessler, W. S., and M. J. McPhaden (1995), Oceanic equatorial waves and the 1991–1993 El Niño, *J. Clim.*, *8*, 1757–1774, doi:10.1175/1520-0442(1995)008<1757:OEWATE>2.0.CO;2.

Kessler, W. S., M. J. McPhaden, and K. M. Weickmann (1995), Forcing of intraseasonal Kelvin waves in the equatorial Pacific, *J. Geophys. Res.*, *100*, 10,613–10,631, doi:10.1029/95JC00382.

Killworth, P. D., and J. R. Blundell (1999), The effect of bottom topography on the speed of long extratropical planetary waves, *J. Phys. Oceanogr.*, *29*, 2689–2710, doi:10.1175/1520-0485(1999)029<2689:TEOBTO>2.0.CO;2.

Large, W., J. McWilliams, and S. Doney (1994), Oceanic vertical mixing: A review and a model with a nonlocal boundary layer parameterization, *Rev. Geophys.*, *32*, 363–403, doi:10.1029/94RG01872.

Lengaigne, M., J.-P. Boulanger, C. Menkes, S. Masson, P. Delecluse, and G. Madec (2002), Ocean response to the March 1997 westerly wind event, *J. Geophys. Res.*, *107*(C12), 8015, doi:10.1029/2001JC000841.

Le Traon, P. Y., F. Nadal, and N. Ducet (1998), An improved mapping method of multisatellite altimeter data, *J. Atmos. Oceanic Technol.*, *15*, 522–534, doi:10.1175/1520-0426(1998)015<0522:AIMMOM>2.0.CO;2.

Locarnini, R. A., et al. (2002), *World Ocean Database 2001*, vol. 4, *Temporal Distribution of Temperature, Salinity and Oxygen Profiles, NOAA Atlas NESDIS*, vol. 45, NOAA, Silver Spring, Md.

Madden, R. A., and P. R. Julian (1971), Detection of a 40–50 day oscillation in the zonal wind field of the tropical Pacific, *J. Atmos. Sci.*, *28*, 702–708, doi:10.1175/1520-0469(1971)028<0702:DOADOI>2.0.CO;2.

Madden, R. A., and P. R. Julian (1972), Description of global-scale circulation cells in the tropics with a 40–50 day period, *J. Atmos. Sci.*, *29*, 1109–1123, doi:10.1175/1520-0469(1972)029<1109:DOGSCC>2.0.CO;2.

Madec, G., P. Delecluse, M. Imbard, and C. Lévy (1998), OPA 8.1 ocean general circulation model reference manual, *Notes Pôle Modél. 11*, Lab. d'Océanogr. Dyn. et de Climatol., Inst. Pierre Simon Laplace, Paris.

Marchesiello, P., and P. Estrade (2010), Upwelling limitation by onshore geostrophic flow, *J. Mar. Res.*, *68*, 37–62, doi:10.1357/002224010793079004.

Marchesiello, P., J. McWilliams, and A. Shchepetkin (2001), Open boundary conditions for long-term integration of regional oceanic models, *Ocean Modell.*, *3*, 1–20, doi:10.1016/S1463-5003(00)00013-5.

Marchesiello, P., J. McWilliams, and A. Shchepetkin (2003), Equilibrium structure and dynamics of the California current system, *J. Phys. Oceanogr.*, *33*, 753–783, doi:10.1175/1520-0485(2003)33<753:ESADOT>2.0.CO;2.

McPhaden, M. J. (1993), TOGA-TAO and the 1991–93 El Niño–Southern Oscillation event, *Oceanography*, *6*, 36–44.

McPhaden, M. J., and B. A. Taft (1988), On the dynamics of seasonal and intraseasonal variability in the eastern equatorial Pacific, *J. Phys. Oceanogr.*, *18*, 1713–1732, doi:10.1175/1520-0485(1988)018<1713:DOSAIV>2.0.CO;2.

McPhaden, M. J., et al. (1998), The Tropical Ocean-Global Atmosphere observing system: A decade of progress, *J. Geophys. Res.*, *103*(C7), 14,169–14,240, doi:10.1029/97JC02906.

Melsom, A., S. D. Meyers, H. E. Hurlburt, E. J. Metzger, and J. J. O'Brien (1999), ENSO effects on Gulf of Alaska eddies, *Earth Interact.*, *3*(1), 1–30, doi:10.1175/1087-3562(1999)003<0001:EEOGOA>2.3.CO;2.

Milliff, R., and J. C. McWilliams (1994), The evolution of boundary pressure in ocean basins, *J. Phys. Oceanogr.*, *24*, 1317–1338, doi:10.1175/1520-0485(1994)024<1317:TEOBPI>2.0.CO;2.

Montecinos, A., O. Leth, and O. Pizarro (2007), Wind-driven interdecadal variability in the eastern tropical and South Pacific, *J. Geophys. Res.*, *112*, C04019, doi:10.1029/2006JC003571.

Montes, I., F. Colas, X. Capet, and W. Schneider (2010), On the pathways of the equatorial subsurface currents in the eastern equatorial Pacific and their contributions to the Peru-Chile Undercurrent, *J. Geophys. Res.*, *115*, C09003, doi:10.1029/2009JC005710.

Montes, I., W. Schneider, F. Colas, B. Blanke, and V. Echevin (2011), Subsurface connections in the eastern tropical Pacific during La Niña 1999–2001 and El Niño 2002–2003, *J. Geophys. Res.*, *116*, C12022, doi:10.1029/2011JC007624.

Penven, P., V. Echevin, J. Pasapera, F. Colas, and J. Tam (2005), Average circulation, seasonal cycle, and mesoscale dynamics of the Peru Current System: A modeling approach, *J. Geophys. Res.*, *110*, C10021, doi:10.1029/2005JC002945.

Penven, P., P. Marchesiello, L. Debreu, and J. Lefevre (2008), Software tools for pre- and post-processing of oceanic regional simulations, *Environ. Model. Software*, *23*, 660–662, doi:10.1016/j.envsoft.2007.07.004.

Pizarro, O., A. J. Clarke, and S. Van Gorder (2001), El Niño sea level and currents along the South American coast: Comparison of observations with theory, *J. Phys. Oceanogr.*, *31*, 1891–1903, doi:10.1175/1520-0485(2001)031<1891:ENOSLA>2.0.CO;2.

Pizarro, O., G. Shaffer, B. Dewitte, and M. Ramos (2002), Dynamics of seasonal and interannual variability of the Peru-Chile Undercurrent, *Geophys. Res. Lett.*, *29*(12), 1581, doi:10.1029/2002GL014790.

Ramos, M., O. Pizarro, L. Bravo, and B. Dewitte (2006), Seasonal variability of the permanent thermocline off northern Chile, *Geophys. Res. Lett.*, *33*, L09608, doi:10.1029/2006GL025882.

Ramos, M., B. Dewitte, O. Pizarro, and G. Garric (2008), Vertical propagation of extratropical Rossby waves during the 1997–1998 El Niño off the west coast of South America in a medium-resolution OGCM simulation, *J. Geophys. Res.*, *113*, C08041, doi:10.1029/2007JC004681.

Renault, L., B. Dewitte, P. Marchesiello, S. Illig, V. Echevin, G. Cambon, M. Ramos, O. Astudillo, P. Minnis, and J. K. Ayers (2012), Upwelling response to atmospheric coastal jets off central Chile: A modeling study of the October 2000 event, *J. Geophys. Res.*, *117*, C02030, doi:10.1029/2011JC007446.

Reynolds, R. W., and T. M. Smith (1994), Improved global sea surface temperature analyses using optimum interpolation, *J. Clim.*, *7*, 929–948, doi:10.1175/1520-0442(1994)007<0929:IGSSTA>2.0.CO;2.

Ridgway, K. R., J. R. Dunn, and J. L. Wilkin (2002), Ocean interpolation by four-dimensional least-squares—Application to the waters around Australia, *J. Atmos. Oceanic Technol.*, *19*(9), 1357–1375, doi:10.1175/1520-0426(2002)019<1357:OIBFDW>2.0.CO;2.

Seiki, A., Y. N. Takayabu, T. Yasuda, N. Sato, C. Takahashi, K. Yoneyama, and R. Shirooka (2011), Westerly wind bursts and their relationship with ENSO in CMIP3 models, *J. Geophys. Res.*, *116*, D03303, doi:10.1029/2010JD015039.

Shaffer, G., O. Pizarro, L. Djurfeldt, S. Salinas, and J. Rutllant (1997), Circulation and low-frequency variability near the Chilean coast: Remotely forced fluctuations during the 1991–1992 El Niño, *J. Phys. Oceanogr.*, *27*, 217–235, doi:10.1175/1520-0485(1997)027<0217:CALFVN>2.0.CO;2.

Shchepetkin, A. F., and J. C. McWilliams (2005), The Regional Oceanic Modeling System: A split-explicit, free-surface, topography-following-coordinate ocean model, *Ocean Modell.*, *9*, 347–404, doi:10.1016/j.ocemod.2004.08.002.

Smith, R., J. K. Dukowicz, and R. C. Malone (1992), Parallel ocean general circulation modelling, *Phys. D*, *60*, 38–61, doi:10.1016/0167-2789(92)90225-C.

Smith, W. H. F., and D. T. Sandwell (1997), Global seafloor topography from satellite altimetry and ship depth soundings, *Science*, *277*, 1956–1962, doi:10.1126/science.277.5334.1956.

Spillane, M. C., D. B. Enfield, and J. S. Allen (1987), Intraseasonal oscillations in sea level along the west coast of the Americas, *J. Phys. Oceanogr.*, *17*, 313–325, doi:10.1175/1520-0485(1987)017<0313:IOISLA>2.0.CO;2.

Stephens, C., et al. (2002), *World Ocean Database 2001*, vol. 3, *Temporal Distribution of Conductivity/Salinity-Temperature-Depth (Pressure) Casts, NOAA Atlas NESDIS*, vol. 44, NOAA, Silver Spring, Md.

Strub, P. T., and C. James (2002), The 1997–1998 oceanic El Niño signal along the southeast and northeast Pacific boundaries—An altimetric view, *Prog. Oceanogr.*, *54*, 439–458, doi:10.1016/S0079-6611(02)00063-0.

Strub, P. T., J. M. Mesias, V. Montecino, J. Rutllant, and S. Salinas (1998), Coastal ocean circulation off western South America, in *The Sea*, vol. 11, edited by A. R. Robinson and K. H. Brink, pp. 273–314, John Wiley, New York.

Tulloch, R., J. Marshall, C. Hill, and K. S. Smith (2011), Scales, growth rates, and spectral fluxes of baroclinic instability in the ocean, *J. Phys. Oceanogr.*, *41*, 1057–1076, doi:10.1175/2011JPO4404.1.

Uppala, S. M., et al. (2005), The ERA-40 reanalysis, *Q. J. R. Meteorol. Soc.*, *131*, 2961–3012, doi:10.1256/qj.04.176.

Vega, A., Y. duPenhoat, B. Dewitte, and O. Pizarro (2003), Equatorial forcing of interannual Rossby waves in the eastern South Pacific, *Geophys. Res. Lett.*, *30*(5), 1197, doi:10.1029/2002GL015886.

Volkov, D., G. Larnicol, and J. Dorandeu (2007), Improving the quality of satellite altimetry data over continental shelves, *J. Geophys. Res.*, *112*, C06020, doi:10.1029/2006JC003765.

Xie, P., and P. A. Arkin (1996), Analysis of global monthly precipitation using gauge observations, satellite estimates, and numerical model predictions, *J. Clim.*, *9*, 840–858, doi:10.1175/1520-0442(1996)009<0840:AOGMPU>2.0.CO;2.

Zamudio, L., A. P. Leonardi, S. D. Meyers, and J. J. O'Brien (2001), ENSO and eddies on the southwest coast of Mexico, *Geophys. Res. Lett.*, *28*(1), 13–16, doi:10.1029/2000GL011814.

Zamudio, L., H. E. Hurlburt, E. J. Metzger, S. L. Morey, J. J. O'Brien, C. E. Tilburg, and J. Zavala-Hidalgo (2006), Interannual variability of Tehuantepec eddies, *J. Geophys. Res.*, *111*, C05001, doi:10.1029/2005JC003182.

Zamudio, L., H. E. Hurlburt, E. J. Metzger, and C. E. Tilburg (2007), Tropical wave-induced oceanic eddies at Cabo Corrientes and the María Islands, Mexico, *J. Geophys. Res.*, *112*, C05048, doi:10.1029/2006JC004018.

A. Belmadani, International Pacific Research Center, School of Ocean and Earth Science and Technology, University of Hawai'i at Mānoa, 1680 East-West Rd., POST Bldg. 401, Honolulu, HI 96822, USA. (belmadan@hawaii.edu)

F. Colas and V. Echevin, LOCEAN/IRD/IPSL/UPMC, 4 Pl. Jussieu, Tour 45-55, F-75005 Paris, France.

B. Dewitte, LEGOS/IRD/OMP/UPS, 14 Ave. Edouard Belin, F-31400 Toulouse, France.